Ocean Modelling 40 (2011) 273–288

Contents lists available at SciVerse ScienceDirect

Ocean Modelling

journal homepage: www.elsevier.com/locate/ocemod

Wave spectral moments and Stokes drift estimation

A. Webb [a,c], B. Fox-Kemper [b,c,*]

[a] Dept. of Applied Mathematics, University of Colorado, Boulder, CO, United States
[b] Dept. of Atmospheric and Oceanic Sciences (ATOC), University of Colorado, Boulder, CO, United States
[c] Cooperative Institute for Research in Environmental Sciences (CIRES), Boulder, CO, United States

ARTICLE INFO

Article history:
Received 10 January 2011
Received in revised form 17 August 2011
Accepted 18 August 2011
Available online 31 August 2011

Keywords:
Wave spectra
Stokes drift
Wave period
Significant wave height

ABSTRACT

The relationships between the moments of wave spectra and Stokes drift velocity are calculated for empirical spectral shapes and a third-generation wave model. From an assumed spectral shape and only an estimate of wave period and significant wave height, one may determine: the leading-order Stokes drift, other wave period estimates, and all spectral moments. The conversion factors are tabulated for quick reference for the common empirical spectral shapes. The different spectral shapes considered are shown to exhibit similar spectral moment relationships. Using these relationships, uncertainty in Stokes drift may be decomposed into the uncertainty in spectral shape and a much greater uncertainty due to significant wave height and wave period discrepancies among ERA40/WAM, satellite altimetry, and CORE2 reanalysis-forced WAVEWATCH III simulations. Furthermore, using ERA40 or CORE2 winds and assuming fully-developed waves results in discrepancies that are unable to explain the discrepancies in modeled Stokes drift; the assumption of fully-developed waves is likely the culprit.

1. Introduction

In situ observations, third-generation wave models, and satellites have begun to provide global estimates of the surface gravity wave field (e.g., Gulev et al., 2003; Caires et al., 2004; Ardhuin et al., 2009a,b; Collard et al., 2009; Hemer et al., 2010; Hanley et al., 2010). The Stokes drift velocity – the mean temporal and spatial difference between the Eulerian and Lagrangian velocities (hereafter Stokes drift) – is useful in calculating the transport of tracers (e.g., McWilliams and Restrepo, 1999) as well as the forcing of surface turbulence (e.g., Craik and Leibovich, 1976; Kantha and Clayson, 2004). However, accuracy and data coverage remain challenges in estimating wave properties, such as Stokes drift, globally. Indeed, McWilliams and Restrepo (1999) chose not to use ocean data in their pioneering global estimation of Stokes drift. At that time, using atmospheric data and the assumption of fully-developed waves (Pierson and Moskowitz, 1964) seemed more reliable than interpolations of buoy and ship data. However, recent climatologies of wave age reveal that assuming equilibration is not trustworthy (Hanley et al., 2010), as often wave state is dominated by developing or remotely-generated swell conditions.

This paper focuses on relationships useful for estimating Stokes drift from diverse ocean wave data sources, so comparisons may reveal persisting errors in data collection and modeling. The challenge in this endeavor is that data storage limitations, for example on buoys or in archived models, often result in loss of complete wave spectral information. Time series of just a few averaged quantities are typically retained, such as mean wave period and significant wave height. In addition, over the past few decades, the wave community has transitioned from an early preference for mean wave period (based on the first moment of frequency) to the zero-crossing wave period (based on the second moment), which provides improved statistical robustness (e.g., Gommenginger et al., 2003). To recover a simplified Stokes drift from these archived records and compare them, the connection between these different mean variables and Stokes drift needs specification.

For deep-water waves of limited steepness, the leading order Stokes drift for monochromatic waves at a specified depth depends inversely on the third power of wave period times the significant wave height squared (e.g., Phillips, 1966). Similarly, for unidirectional (but polychromatic) wave spectra at a specified depth, the Stokes drift depends on the improper integral of the power spectral density divided by the third power of wave period (Kenyon, 1969; McWilliams and Restrepo, 1999).

Dimensional analysis alone may provide a useful scaling for recovering Stokes drift for polychromatic waves with limited data. However, the precise relationship including numerical coefficients depends on the wave period estimate used, which is one indicator of the shape of the wave spectrum. It will be shown that based on knowledge of only a pair of spectral moments and an assumed spectral shape, the Stokes drift and other moments are readily

* Corresponding author at: Dept. of Atmospheric and Oceanic Sciences (ATOC), University of Colorado, Boulder, CO, United States.

E-mail addresses: adrean.webb@colorado.edu (A. Webb), bfk@colorado.edu (B. Fox-Kemper).

1463-5003/$ - see front matter
doi:10.1016/j.ocemod.2011.08.007

estimated and these results are tabulated here. This procedure resembles finding relationships between the mean, variance, skewness, and kurtosis of standard probability distributions. For the wave problem, a spectral shape must be assumed to find these relationships; here well-known empirical spectra and one third-generation model simulation with arbitrary spectral shape (up to limited model resolution) are analyzed. The same calculations can be easily made for other spectra (e.g., Banner, 1990; Alves et al., 2003; Harcourt and D'Asaro, 2008), but are left to the reader or future investigator.

In this paper all Stokes drift approximations use the unidirectional wave assumption, common to other Stokes drift literature (Kenyon, 1969; McWilliams and Restrepo, 1999, etc.).[1] However in our third-generation model, it was found this assumption typically overestimates the leading order Stokes drift (with no wave field assumptions) by about 33% and is briefly addressed in Appendix A.4. Improving estimates of Stokes drift with multi-directional waves is an interesting geometrical problem from our perspective, as wave moments are typically based on scalar quantities, such as surface height variance, while the Stokes drift is a vector quantity. Numerical models easily handle this distinction, but the analysis here does not easily generalize. However, the goal here is an assessment of how well Stokes-related quantities are known and compare among data and models. For this purpose the unidirectional assumption gives a standard, physical, Stokes-related quantity that can be easily compared with limited data.

First this paper reminds the reader of spectral moment definitions and Stokes drift formulae, and then proceeds to evaluate relationships among these properties for different spectral shapes. The notation and conventions of McWilliams and Restrepo (1999) or Bouws (1998) are followed if possible, and other notation and a detailed presentation of Stokes drift is given in the Appendix. Finally, the uncertainty inherent in these approximations is compared to the discrepancies between different ocean wave data products. A forthcoming companion paper (Webb et al., in preparation) describes the climatology of Stokes drift and its relation to surface stress (i.e., the turbulent Langmuir number) over the eight-year window examined here, and the impact of regional variations in this climatology for surface mixing.

2. Spectral moments and observational definitions

It is common to summarize unidirectional or one-dimensional wave spectra at a point by their moments. The moments are defined by Bouws (1998) as

$$m_n = \int_0^\infty f^n \mathcal{S}_f(f)df, \tag{1}$$

where the (*wave*) *frequency spectral density*,[2] $\mathcal{S}_f$, is normalized to capture the variance of the surface height displacement, η, for some time scale T such that[3]

$$\lim_{T\to\infty}\langle\eta(t)^2\rangle_T = \int_0^\infty \mathcal{S}_f(f)df. \tag{2}$$

Similarly, multidirectional or two-dimensional wave spectra can be summarized as

$$\widehat{m_n} = \int_0^\infty \int_{-\pi}^{\pi} f^n \mathcal{S}_{f\theta}(f,\theta)d\theta df, \tag{3}$$

where the *directional-frequency spectral density*, $\mathcal{S}_{f\theta}$, is normalized as

$$\lim_{T,L\to\infty}\langle\eta(\boldsymbol{x}_h,t)^2\rangle_{T,\boldsymbol{L}_h} = \int_0^\infty \int_{-\pi}^{\pi} \mathcal{S}_{f\theta}(f,\theta)d\theta df, \tag{4}$$

for some horizontal length scale $\boldsymbol{L}_h = (L,L)$.[4] By definition,

$$\int_{-\pi}^{\pi} \mathcal{S}_{f\theta}(f,\theta)d\theta \equiv \mathcal{S}_f(f). \tag{5}$$

In practice, wave spectra usually are calculated statistically using expected values for a particular frequency or deterministically as the limit of a finite sum over a limited area, such as a model grid point, as shown in Appendix A.2.2. Since wave amplitude decays exponentially with depth, we expect the 1D and 2D wave moments to decay in z as

$$\begin{aligned}\lim_{T,L\to\infty}\langle\eta_{\tilde z}(\boldsymbol{x}_h,t)^2\rangle_{T,\boldsymbol{L}_h} &= \lim_{T,L\to\infty}\frac{1}{TL^2}\int_{t-T/2}^{t+T/2}\int_{\boldsymbol{x}_h-\boldsymbol{L}_h/2}^{\boldsymbol{x}_h+\boldsymbol{L}_h/2}\eta_{\tilde z}(\boldsymbol{x}',t')^2 d\boldsymbol{x}'dt' && (6)\\ &= \int_0^\infty\int_{-\pi}^{\pi}\mathcal{S}_{f\theta}(f,\theta)e^{\frac{8\pi^2 f^2}{g}z}d\theta df && (7)\\ &= \int_0^\infty \mathcal{S}_f(f)e^{\frac{8\pi^2 f^2}{g}z}df. && (8)\end{aligned}$$

The decay with depth depends on wavenumber k or real frequency f, here related by the dispersion relation for linear deep-water waves ($4\pi^2 f^2 = gk$), where g is the gravitational acceleration.

1D spectral moments are used to define traditional measures of wave properties clearly. The *spectral significant wave height*, H_{m0}, is a commonly used measure of wave height and is similar in magnitude to the *observed significant wave height*, $\overline{H}_{1/3}$.[5] It is defined as $H_{m0} = 4\sqrt{m_0}$ and typically ranges from $1.015\overline{H}_{1/3}$ to $1.08\overline{H}_{1/3}$ in wave observations (Ochi, 1998). Likewise, the ratios of moments, T_n, with dimensions in time given below, can be used to approximate the *mean wave period* $\overline{T}_m$ and *zero-crossing wave period* $\overline{T}_z$ (see Gommenginger et al., 2003)

$$T_n = \left(\frac{m_0}{m_n}\right)^{\frac{1}{n}}; \quad \overline{T}_m \approx \frac{m_0}{m_1}, \quad \overline{T}_z \approx \left(\frac{m_0}{m_2}\right)^{\frac{1}{2}}. \tag{9}$$

NOAA WAVEWATCH III (abbreviated here as WW3) commonly saves T_{-1} (Tolman, 2009, p. 38). In calculating the surface Stokes drift, T_3 is ideal (see (13)). Often the spectrum is sharply peaked at a particular wave period, this period is known as the (*spectral*) *peak wave period*.

Significant wave height and one or more mean period estimates are often the only spectral data retained due to limited memory or estimated empirically (e.g., Gommenginger et al., 2003). Similar conventions apply to *mean wavelength*, where moments of the spectral distribution as a function of wavenumber are used.

With only limited spectral information, it may still be possible to estimate the Stokes drift accurately. The leading-order expression for the *full Stokes drift*, $\boldsymbol{u}^S$, from an arbitrary spectral shape is derived in the Appendix and given as

$$\boldsymbol{u}^S = \frac{16\pi^3}{g}\int_0^\infty\int_{-\pi}^{\pi}(\cos\theta,\sin\theta,0)f^3\mathcal{S}_{f\theta}(f,\theta)e^{\frac{8\pi^2 f^2}{g}z}d\theta df. \tag{10}$$

Notice that the horizontally-two-dimensional (henceforth $2D_h$) Stokes drift is a vector quantity whose magnitude depends both on the directional components of the wave field and the directional spread of wave energy (based on $\mathcal{S}_{f\theta}$) for each component. This can be quite complicated to estimate; however, a simpler unidirectional

[1] The unidirectional assumption supposes that there is a single wave direction for waves of all frequencies, so that wave direction can be neglected when calculations involving integration over frequency are performed. This assumption is *stronger* than the assumption of a typical wave direction with a spreading function about it (e.g., as in Donelan et al. (1985)). It will be required to go from (10) and (11).

[2] f is ordinary (not angular) wave frequency.

[3] Angle brackets denote spatial or temporal averaging as indicated by the subscripts.

[4] The h subscript denotes horizontal components.

[5] Hereafter, the *significant wave height* will refer to the *spectral significant wave height*, H_{m0}, unless otherwise specified.

or horizontally-one-dimensional (henceforth $1D_h$) form of Stokes drift and its surface value ($\boldsymbol{u}^s$ and $\boldsymbol{U}^s$, respectively) result if the wave spectra are assumed to be separable into wave direction and frequency components and the waves are unidirectional (see Kenyon, 1969; McWilliams and Restrepo, 1999, and the Appendix):

$$\boldsymbol{u}^s = \hat{\boldsymbol{e}}^w \frac{16\pi^3}{g} \int_0^\infty f^3 \mathcal{S}_f(f) e^{\frac{8\pi^2 f^2}{g} z} \, df, \tag{11}$$

$$\boldsymbol{U}^s \equiv \boldsymbol{u}^s|_{z=0} = \hat{\boldsymbol{e}}^w \frac{16\pi^3}{g} \int_0^\infty f^3 \mathcal{S}_f(f) \, df \tag{12}$$

$$= \hat{\boldsymbol{e}}^w \frac{16\pi^3 m_3}{g}. \tag{13}$$

In this common simplification the assumed wave direction is given by $\hat{\boldsymbol{e}}^w$.

Thus, only the third moment of the 1D wave spectrum, m_3, is required to estimate the $1D_h$ surface Stokes drift, and the third moment is usually related to available data. For example, given only T_3 and H_{m0}, and the definitions above,

$$\boldsymbol{U}^s = \hat{\boldsymbol{e}}^w \frac{\pi^3 (16 m_0)}{g (m_0/m_3)} = \hat{\boldsymbol{e}}^w \frac{\pi^3 H_{m0}^2}{g T_3^3}. \tag{14}$$

If T_3 was routinely saved in data, it would be straightforward to estimate the $1D_h$ surface Stokes drift. However, T_3 is uncommon in archived data, in comparison to T_1 and T_2, so conversions among these 1D moments are valuable. In the following section, relationships between these mean periods are found in prototypical 1D wave spectra and WW3 simulations. In later sections, it also will be shown that the $1D_h$ depth-dependent Stokes drift, $\boldsymbol{u}^s$, may be estimated at depths other than the surface, and again spectral shape information is needed in addition to a pair of spectral moments.

3. Comparing empirical and model-generated wave spectra

3.1. Monochromatic waves

The simplest spectrum is a monochromatic one: composed of a single frequency and wavenumber, e.g., $\eta = a\cos(kx - \omega t)$. The only wave frequency is the peak wave frequency, given by $2\pi f_p = \sqrt{gk}$. All energy in the spectrum is concentrated at this frequency, so $\mathcal{S}_{f,\delta}(f) = \frac{a^2}{2}\delta(f - f_p)$. The moments and mean periods are

$$m_{n,\delta} = \int_0^\infty f^n \mathcal{S}_{f,\delta}(f) df = \int_0^\infty f^n \frac{a^2}{2} \delta(f - f_p) df = \frac{a^2}{2} f_p^n, \tag{15}$$

$$T_{n,\delta} = \left(\frac{m_{0,\delta}}{m_{n,\delta}}\right)^{(1/n)} = 1/f_p. \tag{16}$$

The $1D_h$ Stokes drift, from (11), is

$$\boldsymbol{u}^s_\delta(z) = \hat{\boldsymbol{e}}^w \frac{16\pi^3}{g} \int_0^\infty f^3 \mathcal{S}_{f,\delta}(f) e^{\frac{8\pi^2 f^2}{g} z} df \tag{17}$$

$$= \hat{\boldsymbol{e}}^w \frac{16\pi^3}{g} \int_0^\infty f^3 \frac{a^2}{2} \delta(f - f_p) e^{\frac{8\pi^2 f^2}{g} z} df \tag{18}$$

$$= \hat{\boldsymbol{e}}^w \frac{8\pi^3 a^2 f_p^3}{g} e^{\frac{8\pi^2 f_p^2}{g} z} \tag{19}$$

$$= \hat{\boldsymbol{e}}^w a^2 \sqrt{g k^3} e^{2kz}. \tag{20}$$

The result in (20) is the standard result for linear deep-water (e.g., Phillips, 1966; Kundu, 1990).

3.2. Pierson and Moskowitz spectrum

Pierson and Moskowitz (1964, PM hereafter) proposed the following fit of wave spectra for fully developed seas, following the ideas of Phillips (1958):

$$\mathcal{S}_f(f) = \mathcal{S}_{f,PM}(f) = \frac{\alpha_{PM} g^2}{(2\pi)^4 f^5} \exp\left[-\frac{5}{4}\left(\frac{f_p}{f}\right)^4\right]. \tag{21}$$

This spectrum has the moments

$$m_{n,PM} = \frac{\alpha_{PM} g^2 \left(\frac{5}{4}\right)^{\frac{n}{4}} \Gamma\left(1 - \frac{n}{4}\right)}{80\pi^4 f_p^{4-n}}, \quad \text{for } -1 \leqslant n \leqslant 3, \tag{22}$$

and thus the mean periods

$$T_{n,PM} = f_p^{-1} \frac{\left(\frac{4}{5}\right)^{\frac{1}{4}}}{\Gamma\left(1 - \frac{n}{4}\right)^{\frac{1}{n}}}, \quad \text{for } -1 \leqslant n \leqslant 3. \tag{23}$$

Numerical results for the spectral moments and mean periods for the PM spectrum are found in Tables 1 and 2. Along with (13), the $1D_h$ Stokes drift can be calculated from these tables. The surface magnitude is

$$U^s_{PM} = \frac{\Gamma\left(\frac{5}{4}\right)}{\pi\left(\frac{5}{4}\right)^{\frac{1}{4}}} \frac{g\alpha_{PM}}{f_p} = (0.273\ldots) \frac{g\alpha_{PM}}{f_p}. \tag{24}$$

Tables 1 and 2 show that, as dimensional analysis would predict, the ratio of the moments and wave period estimates of the PM spectrum depend on the same power of peak frequency as the monochromatic spectrum. However, these moment ratios differ by a numerical factor, which ranges from 0.86 to 4.3 times the monochromatic ratios. These numerical factors reflect the energy in the PM spectrum at periods other than the peak wave period.

For fully-developed wave conditions the remaining parameters in the PM spectrum are estimated empirically (Bouws, 1998), although the calculations above do not rely on these approximations. That is, only the spectral shape of the PM theory is kept, not the assumption of fully-developed waves.[6] Typical values for fully-developed waves are $\alpha_{PM} = 8.1 \times 10^{-3}$, $f_p = \left(\frac{5}{4\beta}\right)^{1/4} \frac{g}{2\pi U_{19.5}}$ with $\beta = 0.74$, where $U_{19.5}$ is the wind speed at 19.5 m above the sea surface. The magnitude of the $1D_h$ surface Stokes drift velocity is $U^s_{PM} = 0.0158 U_{19.5}$. Assuming a neutrally stable atmospheric boundary layer and a drag coefficient of 1.3×10^{-3}, then $U_{19.5} \approx 1.026 U_{10}$ (wind speed at 10 m above the sea surface) (Stewart, 2008) and

$$U^s_{PM} \approx 0.0162 U_{10}. \tag{25}$$

3.3. JONSWAP spectrum

A primary result of the Joint North Sea Wave Observation Project (JONSWAP: Hasselmann and Olbers, 1973; Hasselmann et al., 1976) is the effect of a finite fetch, F, to represent incomplete wave development. Introducing this development changes the PM spectrum to have the potential for a sharper spectral peak near the peak frequency, and an evolving amplitude:

$$\mathcal{S}_f(f) = \mathcal{S}_{f,J}(f) = \frac{\alpha_J g^2}{(2\pi)^4 f^5} \exp\left[-\frac{5}{4}\left(\frac{f_p}{f}\right)^4\right] (\gamma_J)^{\Gamma_J}, \tag{26}$$

$$\Gamma_J = \exp\left[-\frac{(f - f_p)^2}{2\sigma_J^2 f_p^2}\right]. \tag{27}$$

The empirical parameters that are required for the calculations here are σ_J and the peak enhancement factor γ_J, which are used to numerically integrate over the spectral shape:

$$\gamma_J = 3.3, \tag{28}$$

[6] Of course, the spectral shape was found also by arguments and observations related to fully-developed seas.

Table 1
Moment ratios for different spectra.

	$m_0 = H_{m0}^2/16$	m_{-1}/m_0	m_1/m_0	m_2/m_0	m_3/m_0
Mono	$a^2/2$	f_p^{-1}	f_p	f_p^2	f_p^3
JONSWAP	$0.31g^2\alpha_J(2\pi f_p)^{-4}$	$0.90f_p^{-1}$	$1.2f_p$	$1.7f_p^2$	$3.2f_p^3$
PM	$\frac{1}{5}g^2\alpha_{PM}(2\pi f_p)^{-4} = (0.200\ldots)g^2\alpha_{PM}(2\pi f_p)^{-4}$	$\Gamma(\frac{5}{4})(\frac{4}{5})^{\frac{1}{4}}f_p^{-1} = (0.8572\ldots)f_p^{-1}$	$\Gamma(\frac{3}{4})(\frac{5}{4})^{\frac{1}{4}}f_p = (1.296\ldots)f_p$	$\sqrt{5\pi/4}f_p^2 = (1.982\ldots)f_p^2$	$\Gamma(\frac{1}{4})(\frac{5}{4})^{\frac{3}{4}}f_p^3 = (4.289\ldots)f_p^3$
$\langle$WW3$\rangle_{G,T}$	0.658 m^2 = (3.24 m)^2/16	8.97 s = (0.111 s^{-1})$^{-1}$	0.137 s^{-1}	0.0257 s^{-2} = (0.160 s^{-1})^2	0.00800 s^{-3} = (0.200 s^{-1})^3

Table 2
Period ratios for different spectra.

	T_3	T_{-1}/T_3	T_1/T_3	T_2/T_3	T_{-1}/T_2	T_1/T_2	T_{-1}/T_1
Mono	f_p^{-1}	1	1	1	1	1	1
JONSWAP	$0.680f_p^{-1}$	1.33	1.23	1.14	1.16	1.07	1.08
PM	$(\frac{5}{4})^{-\frac{1}{4}}\Gamma(\frac{1}{4})^{-\frac{1}{3}}f_p^{-1} = (0.6156\ldots)f_p^{-1}$	$\frac{1}{4}\Gamma(\frac{1}{4})^{\frac{4}{3}} = 1.392\ldots$	$\frac{1}{\sqrt{2\pi}}\Gamma(\frac{1}{4})^{\frac{4}{3}} = 1.254..$	$\pi^{-\frac{1}{4}}\Gamma(\frac{1}{4})^{\frac{1}{3}} = 1.154\ldots$	$\frac{1}{4}\pi^{\frac{1}{4}}\Gamma(\frac{1}{4}) = 1.207\ldots$	$\frac{1}{\sqrt{2}\pi^{\frac{3}{4}}}\Gamma(\frac{1}{4}) = 1.086\ldots$	$2^{-\frac{3}{2}}\pi = 1.111\ldots$
$\langle$WW3$\rangle_{G,T}$	5.58 s	1.63	1.37	1.21	1.34	1.13	1.18

$$\sigma_J = \begin{cases} 0.07, & f \leqslant f_p, \\ 0.09, & f > f_p. \end{cases} \tag{29}$$

Analytic integration is not as easy in the JONSWAP spectrum as for the PM spectrum, due to the $(\gamma_J)^{\Gamma_J}$ term. However, the moments and periods can be evaluated numerically – without specifying additional parameters – by utilizing a change of variables and removing f_p from the integrand prior to integration (Tables 1 and 2). The resulting 1D$_h$ surface Stokes drift magnitude is

$$U_J^s \approx 0.316\frac{g\alpha_J}{f_p}, \tag{30}$$

which is 16% higher than the PM spectrum with matching Phillips constant (i.e., $\alpha_{PM} = \alpha_J$) and peak frequency. However, a more apt comparison is found by matching significant wave height and peak frequency, in which case $\alpha_J = 0.65\alpha_{PM}$ (Table 1), and the 1D$_h$ surface Stokes drift from the JONSWAP spectrum is then only 75% that of the PM spectrum.

The spectral peak frequency, f_p, and other constants are empirically determined to be (Stewart, 2008):

$$f_p = 22\left(\frac{g^2}{U_{10}F}\right)^{1/3}, \quad \alpha_J = 0.076\left(\frac{U_{10}^2}{F\,g}\right)^{0.22}. \tag{31}$$

F is the fetch, the distance over which wind blows with a constant velocity. For reference, the relationship between the JONSWAP 1D$_h$ surface Stokes drift magnitude and U_{10} velocity is

$$U_J^s = 1.60 \times 10^{-5}\ F^{17/150}U_{10}^{58/75}. \tag{32}$$

3.4. Donelan et al. (1985) spectrum

Donelan et al. (1985) propose an alternative to the basic spectral form used by PM and JONSWAP. It is

$$\mathcal{S}_f(f) = \mathcal{S}_{f,DHH}(f) = \frac{\alpha_{DHH}g^2}{(2\pi)^4 f^4 f_p}\exp\left[-\left(\frac{f_p}{f}\right)^4\right](\gamma_{DHH})^{\Gamma_{DHH}}. \tag{33}$$

This spectrum will be called the DHH spectrum below. The crucial difference of the DHH spectrum from the JONSWAP spectrum is the f^{-4} tail at high frequencies instead of the f^{-5} tail used by the preceding spectra. This scaling has strong observational (see Banner, 1990; Alves et al., 2003, for lists) and theoretical support (Kitaigorodskii, 1983), and a related wavenumber spectrum is proposed by Banner (1990).

The DHH spectrum parameters differ slightly from JONSWAP as well:

$$\gamma_{DHH} = \begin{cases} 1.7, & 0.83 < \frac{U_{10}}{c_p} < 1, \\ 1.7 + 6.0\log_{10}\left(\frac{U_{10}}{c_p}\right), & 1 < \frac{U_{10}}{c_p} < 5, \end{cases} \tag{34}$$

$$\Gamma_{DHH} = \exp\left[-\frac{(f-f_p)^2}{2\sigma_{DHH}^2 f_p^2}\right], \tag{35}$$

$$\sigma_{DHH} = 0.08\left[1 + 4\left(\frac{U_{10}}{c_p}\right)^{-3}\right]. \tag{36}$$

The peak enhancement factor is now a function of inverse wave age (U_{10}/c_p).[7] Since we will have to numerically integrate over the peak enhancement, this means that multiple results for different wave ages will be tabulated. Following Donelan et al. (1985), fetch-limited ($U_{10}/c_p = 4$, $\gamma_{DHH} = 5.3$) and fully-developed ($U_{10}/c_p = 0.83$, $\gamma_{DHH} = 1.7$) cases will be used.

The difficulty with this spectrum in the present development is that the surface Stokes drift and third moment do not converge as f approaches infinity, as the integral in (11) is unbounded. In reality, Stokes drift convergence may result from different spectral behavior for the shortest waves (Banner, 1990, notes a number of observational studies where the spectrum far above the peak frequency varies widely). Or, perhaps the approximation for Stokes drift (11) breaks down as k increases, for example as viscosity becomes important (e.g., Komen, 1987). In either case, Section 5 demonstrates that these convergence issues do not arise for *subsurface* Stokes drift, where the decay of short waves with depth makes longer waves increasingly dominant. Indeed, at only *one percent of the e-folding depth of the peak wave*, the Stokes drift from the DHH spectrum is easily calculated (Tables 4 and 5). At half the peak wave e-folding depth and deeper, the fetch-limited version of the DHH spectrum is very close to JONSWAP and the fully-developed DHH spectrum is very close to PM, so the spectral tail is indeed inconsequential for wave spectra at moderate and greater depths. However, the surface values of Stokes drift and third moment differ substantially, and thus the Donelan et al. (1985) surface spectrum will not be presented.

[7] This quantity is called wave age, as young waves tend to form with $U_{10} > c_p$, that is, with the component of wave phase speed in the wind direction lagging behind the wind. As the waves age, longer, faster wavelengths are energized so that the wave speed rivals the wind speed.

Table 3
Proposed coefficient for the monochromatic surface Stokes drift form using different mean periods.

	$a_{-1} = U^s/D_{-1}$	$a_1 = U^s/D_1$	$a_2 = U^s/D_2$	$a_3 = U^s/D_3$
Mono	1	1	1	1
JONSWAP	2.34	1.84	1.49	1
PM	2.700...	1.970...	1.537...	1
$\langle$WW3$\rangle_{G,T}$	3.34	2.31	1.69	1

3.5. Model-generated wave spectrum

WW3 is an operational third-generation wave model that calculates and uses 2D wave spectra to forecast the ocean wave state. Here, version 2.22 of the model with corresponding operational settings was used to generate output every 6 h for the period 1994–2001. Some of the operational settings include 25 frequency and 24 directional bins (with an initial and cutoff frequency of 0.0418 and 0.411, respectively), f^{-5} tail, 3rd order propagation scheme, and Tolman and Chalikov source terms (for full details, see http://polar.ncep.noaa.gov/waves/implementations.shtml). This WW3 simulation was forced with CORE2 (Large and Yeager, 2008) winds[8] with appropriate sea surface temperatures (Hadley SST: Rayner et al., 2006) and sea ice concentrations (Bootstrap Sea Ice Concentrations from Nimbus-7 SMMR and DMSP SSM/I: v2 (Comiso, 1999)) on a $1^\circ \times 1.25^\circ$ latitude-longitude grid of $(-78{:}78) \times (0{:}358.75)$, respectively. A 50% sea ice threshold for grid point inclusion was used for all temporal means (temporal means taken over eight years total, denoted $\langle\cdot\rangle_T$) and an area-weighted global mean (denoted $\langle\cdot\rangle_G$) accounts for changing meridians with latitude.

In Tables 1–3, calculations using wave spectra from this WW3 simulation are compared with the analytic results based on the PM and JONSWAP spectral shapes. Typically, the values used in the tables (with the exception of Table 3)[9] are spatial and temporal means over the eight years of six-hourly snapshots.

4. Example comparisons of data and models

4.1. Different 1D$_h$ spectra

The different 1D spectra in Tables 1–3, PM, JONSWAP and WW3, are designed to have a roughly similar shape. All feature a similar rolloff at high frequencies, for example, while the DHH spectrum has a less steep rolloff slope. However, the detailed differences between the spectra result in different moments and 1D$_h$ Stokes drift for the same peak frequency and significant wave height.[10]

Table 1 compares the moments of the different spectra. Higher moments emphasize the energy at higher frequencies, and lower moments emphasize lower frequencies. The results in Table 1 indicate that both PM and JONSWAP are skewed toward higher frequency energy when compared to a monochromatic spectrum of the same peak frequency. The PM spectrum has less energy near the peak frequency than JONSWAP and therefore has larger higher moments for the same significant wave height. The WW3 moments are skewed toward higher frequencies at higher moments as well, which is indicated by the increasing numerical frequency with increasing n of the moment in the bottom row of the table. The analytic spectra have the same proportionality to peak wave period as the monochromatic spectrum, but it would be very misleading to assume that the surface spectral moments of the wave spectra are equal to the monochromatic moments. Indeed, the m_3/m_0 ratio differs by more than a factor of three from the monochromatic estimate.

Table 2 compares the mean period estimates T_n of the spectra based on different moments from (9). As higher moments are skewed toward higher frequencies (and thus lower periods), the period estimates based on higher moments tend to be shorter than those based on lower moments. The scalings are similar between the three spectra, but WW3 is farthest from the monochromatic result and JONSWAP is nearest, consistent with its peaked shape near the peak frequency.

4.2. Revisiting the 1D$_h$ surface Stokes drift of monochromatic waves

The simplest spectrum is a monochromatic one. In this case, there is only one wave period, the peak period, and all T_n yield the same answer. Then (20) at the surface yields the relation

$$\boldsymbol{U}^s_\delta = \hat{\boldsymbol{e}}^w a^2\sqrt{gk^3} = \hat{\boldsymbol{e}}^w \frac{\pi^3(16a^2/2)}{g/f_p^3} = \hat{\boldsymbol{e}}^w \frac{\pi^3 H_{m0}^2}{gT_n^3}. \quad (37)$$

Note that the power law dependence on period T_n and significant wave height of this simple formula can be reused as an approximation, because it is exactly the same as that found with T_3 and H_{m0} in (14) for a generic 1D wave spectrum. For notational simplicity, let D_n denote the monochromatic form for the 1D$_h$ surface Stokes drift velocity, based on the nth period estimate from an observed wave spectrum:

$$D_n = \frac{\pi^3 H_{m0}^2}{gT_n^3}. \quad (38)$$

For a given spectral shape, the moments and period estimates are known (Tables 1 and 2). Using a given spectral shape, it is clear that we can choose a_n such that

$$U^s \approx a_n D_n. \quad (39)$$

The approximation for the polychromatic spectra will be $\boldsymbol{U}^s \approx \hat{\boldsymbol{e}}^w a_n D_n$, where a_n is a dimensionless constant based on the assumed 1D spectral shape. It is clear from Table 2 that using the monochromatic wave Stokes drift will only agree with (i.e., $a_n = 1$) for real wave spectra if $n = 3$. Then, the 1D$_h$ surface Stokes drift magnitude is $U^s = D_3$ from (14). If a different period estimate is used, it will be based on different moments other than the 3rd moment, and $a_n \neq 1$.

Best estimates for a_n are given in Table 3. The values for WW3 were determined using a linear weighted least squares fit to minimize the global-mean-square error. Noticeably, the different spectral shapes produce different values. Indeed, the reason why multiple 1D spectra are used here is to exemplify a realistic range of values. The estimate $a_{-1}D_{-1}$ is not reliable for U^s, as it depends sensitively on wave spectrum shape (>40%). However, for $n = 1$, the estimates differ by about 23%, for $n = 2$ by less than 13%. While this uncertainty is not negligible, it will be shown in Section 6 that it is modest when compared to the present discrepancy in Stokes drift estimates between different data sources. All of the empirical spectra have more Stokes drift than a monochromatic spectrum with the same peak frequency and significant wave height, because Stokes drift tends to be larger for higher frequencies in (11) and these empirical spectra have power at higher frequencies. Since PM is less peaked than JONSWAP, it has larger a_n values. Apparently WW3 has even more relative high-frequency energy, as it has the highest values of a_n.

It is perhaps more direct to describe this monochromatic approximation as a process to determine the peak frequency and amplitude required to find the Stokes drift in (30) and (24) from

[8] Available from http://data1.gfdl.noaa.gov/nomads/forms/mom4/COREv2.html.
[9] See Section 4.2.
[10] While the numerical model frequency bins are of limited resolution, experimentation with reducing the high frequency cutoff by up to 28% changed estimates of Stokes drift by less than 10%.

the observed spectral moments. The amplitude naturally is found from the significant wave height or zeroth moment, and then different period estimates are used to estimate the peak frequency. In addition to estimating Stokes drift, if one assumes a spectral shape (PM or JONSWAP), then using Tables 1, 2 and H_{m0} or m_0 and *any other* moment or period estimate, the remaining moments, period estimates, and spectral parameters can be calculated. All that is required is (1) determination of α_J or α_{PM} as a function of f_p from the first column of Table 2, and (2) determination of f_p from the relevant columns of Table 2 if a period estimate is provided or column of Table 1 if a spectral moment is provided.

5. 1D$_h$ subsurface Stokes drift

The preceding discussion has focused on estimating the 1D$_h$ surface Stokes drift. However, it is often the case that the value of the Stokes drift at depth is needed (e.g., Harcourt and D'Asaro, 2008). Here the behavior at the nth e-folding depth of the peak frequency wave is chosen for illustration $\left(z_n = -ng/\left(8\pi^3 f_p^2\right)\right)$. At this depth the Stokes drift and moments at each frequency are attenuated by $\exp\left[-nf^2/f_p^2\right]$.

While a monochromatic algebraic form is useful for estimating the surface Stokes drift in (14), this estimation does not imply that the monochromatic spectrum is a good estimate of other wave characteristics. In particular, the subsurface Stokes drift of realistic spectra decays much more quickly with depth than the Stokes drift of a monochromatic spectrum with the same surface moments. Table 4 compares the 1D$_h$ Stokes drift magnitudes at depth depending on the surface spectrum,

$$|\boldsymbol{u}^s(z)| \equiv \mathsf{b}_n(z) D_n(z_0). \tag{40}$$

The superexponential decay of the overall Stokes drift (i.e., $\mathsf{b}_n(z_n) \ll \exp[-n]$) in the realistic spectra results from the faster exponential decay of waves with shorter period than T_3. Indeed, the $\mathsf{b}_n(z_0)$ values are all greater than one, but the b_n values drop off more quickly than e^{-n} with increasing depth. Thus, the $D_n(z_0)$ need strengthening over a monochromatic spectrum to arrive at the surface Stokes drift, but by half an e-folding depth, the $D_n(z_{1/2})$ need weakening to arrive at the subsurface Stokes drift (Tables 4 and 5). So, the Stokes drift of the monochromatic spectrum (Eqs. (17)–(20)), which decays only exponentially, overestimates the Stokes drift of the realistic spectra at depth. Note that the Stokes drift of the DHH spectrum, which has the largest concentration of energy at high frequency of the spectra considered, decreases most quickly with depth.

If one happened to have observational data containing the moments or wave period estimates at depth, then similar formulae to the ones for surface Stokes drift may be used. For example, while the spectrum at depth $\mathcal{S}_f(f,z)$ differs from the surface spectrum $\mathcal{S}_f(f)$, similar relationships to (14) hold among the subsurface properties

$$\mathcal{S}_f(f,z) = \mathcal{S}_f(f) e^{\frac{8\pi^2 f^2}{g} z}, \tag{41}$$

$$m_n(z) = \int_0^\infty f^n \mathcal{S}_f(f,z) df, \tag{42}$$

$$\boldsymbol{u}^s(z) = \hat{\boldsymbol{e}}^w \frac{16\pi^3}{g} \int_0^\infty f^3 \mathcal{S}_f(f,z)\, df \tag{43}$$

$$= \hat{\boldsymbol{e}}^w \frac{\pi^3(16 m_0(z))}{g(m_0(z)/m_3(z))} = \hat{\boldsymbol{e}}^w \frac{\pi^3 [H_{m0}(z)]^2}{g[T_3(z)]^3}. \tag{44}$$

Interestingly, as the higher-frequency modes decay with depth, the spectrum becomes more peaked near the peak frequency and thus the monochromatic form *based on moments at depth* becomes more accurate (Table 5):

$$D_n(z) = \frac{\pi^3 [H_{m0}(z)]^2}{g[T_n(z)]^3}, \tag{45}$$

$$|\boldsymbol{u}^s(z)| \equiv \mathsf{a}_n(z) D_n(z). \tag{46}$$

The crucial distinction between the $\mathsf{a}_n(z)$ (Table 5) and $\mathsf{b}_n(z)$ (Table 4) is that having data at depth captures the superexponential decay of the realistic wave spectra.

Fig. 1 illustrates the converging spectral shapes with depth. It is clear that the DHH spectrum with inverse wave age of 4 closely resembles the JONSWAP spectrum, while the DHH spectrum with inverse wave age of 0.83 closely resembles the PM spectrum. The biggest differences are in the high frequency spectral tails in the near-surface spectra (Fig. 1a). These tails are shallower for the DHH spectra (nearly proportional to $(f/f_p)^{-4}$) than for the JONSWAP and PM spectra (nearly proportional to $(f/f_p)^{-5}$). At a slightly greater depth ($z_{1/2}$), these spectral tails have been strongly attenuated

Table 4
Subsurface Stokes drift coefficients with surface moments at Stokes drift e-folding depths of the spectral peak wave $\left(z_n = -ng\Big/\left(8\pi^2 f_p^2\right)\right)$.

	$\mathsf{b}_{-1}(z) = \lvert\boldsymbol{u}^s(z)\rvert/D_{-1}(z_0)$	$\mathsf{b}_1(z) = \lvert\boldsymbol{u}^s(z)\rvert/D_1(z_0)$	$\mathsf{b}_2(z) = \lvert\boldsymbol{u}^s(z)\rvert/D_2(z_0)$	$\mathsf{b}_3(z) = \lvert\boldsymbol{u}^s(z)\rvert/D_3(z_0)$
PM (z_0)	2.700...	1.970...	1.537...	1
PM ($z_{0.01}$)	$2.20e^{-0.01}$	$1.61e^{-0.01}$	$1.25e^{-0.01}$	$0.82e^{-0.01}$
PM ($z_{1/2}$)	$(0.791\ldots)e^{-1/2}$	$(0.578\ldots)\, e^{-1/2}$	$(0.450\ldots)e^{-1/2}$	$(0.293\ldots)e^{-1/2}$
PM (z_1)	$(0.562\ldots)e^{-1}$	$(0.410\ldots)e^{-1}$	$(0.320\ldots)e^{-1}$	$(0.208\ldots)e^{-1}$
PM (z_2)	$(0.420\ldots)e^{-2}$	$(0.306\ldots)e^{-2}$	$(0.239\ldots)e^{-2}$	$(0.155\ldots)e^{-2}$
PM (z_3)	$(0.394\ldots)e^{-3}$	$(0.288\ldots)e^{-3}$	$(0.224\ldots)e^{-3}$	$(0.146\ldots)e^{-3}$
JONSWAP (z_0)	2.34	1.84	1.49	1
JONSWAP ($z_{0.01}$)	$1.96e^{-0.01}$	$1.54e^{-0.01}$	$1.25e^{-0.01}$	$0.837e^{-0.01}$
JONSWAP ($z_{1/2}$)	$0.868e^{-1/2}$	$0.683e^{-1/2}$	$0.553e^{-1/2}$	$0.371e^{-1/2}$
JONSWAP (z_1)	$0.685e^{-1}$	$0.540e^{-1}$	$0.437e^{-1}$	$0.293e^{-1}$
JONSWAP (z_2)	$0.569e^{-2}$	$0.448e^{-2}$	$0.363e^{-2}$	$0.243e^{-2}$
JONSWAP (z_3)	$0.546e^{-3}$	$0.431e^{-3}$	$0.348e^{-3}$	$0.234e^{-3}$
DHH ($U_{10}/c_p = 0.83, z_{0.01}$)	$2.85e^{-0.01}$	$1.89\, e^{-0.01}$	$1.21e^{-0.01}$	n/a
DHH ($U_{10}/c_p = 4, z_{0.01}$)	$2.95e^{-0.01}$	$2.03\, e^{-0.01}$	$1.27e^{-0.01}$	n/a
DHH ($U_{10}/c_p = 0.83, z_{1/2}$)	$0.683e^{-1/2}$	$0.453\, e^{-1/2}$	$0.290e^{-1/2}$	n/a
DHH ($U_{10}/c_p = 4, z_{1/2}$)	$0.772e^{-1/2}$	$0.529\, e^{-1/2}$	$0.331e^{-1/2}$	n/a
DHH ($U_{10}/c_p = 0.83, z_1$)	$0.457e^{-1}$	$0.303e^{-1}$	$0.194e^{-1}$	n/a
DHH ($U_{10}/c_p = 4, z_1$)	$0.586e^{-1}$	$0.402e^{-1}$	$0.252e^{-1}$	n/a
DHH ($U_{10}/c_p = 0.83, z_2$)	$0.315e^{-2}$	$0.209e^{-2}$	$0.133e^{-2}$	n/a
DHH ($U_{10}/c_p = 4, z_2$)	$0.478e^{-2}$	$0.328e^{-2}$	$0.205e^{-2}$	n/a
DHH ($U_{10}/c_p = 0.83, z_3$)	$0.279e^{-3}$	$0.185e^{-3}$	$0.118e^{-3}$	n/a
DHH ($U_{10}/c_p = 4, z_3$)	$0.453e^{-3}$	$0.311e^{-3}$	$0.194e^{-3}$	n/a
Mono (z_n)	e^{-n}	e^{-n}	e^{-n}	e^{-n}

Table 5
Subsurface Stokes drift coefficients with known moments at e-folding depths of the spectral peak wave $\left(z_n = -ng \Big/ \left(8\pi^2 f_p^2\right)\right)$.

	$a_{-1}(z) = \lvert \boldsymbol{u}^s(z)\rvert / D_{-1}(z)$	$a_1(z) = \lvert \boldsymbol{u}^s(z)\rvert / D_1(z)$	$a_2(z) = \lvert \boldsymbol{u}^s(z)\rvert / D_2(z)$	$a_3(z) = \lvert \boldsymbol{u}^s(z)\rvert / D_3(z)$
WW3 (z_0)	3.34	2.31	1.69	1
PM (z_0)	2.700...	1.970...	1.537...	1
PM ($z_{0.01}$)	2.25	1.67	1.35	1
PM ($z_{1/2}$)	1.39	1.20	1.10	1
PM (z_1)	1.28	1.14	1.07	1
PM (z_2)	1.19	1.10	1.05	1
PM (z_3)	1.15	1.08	1.04	1
JONSWAP (z_0)	2.34	1.84	1.49	1
JONSWAP ($z_{0.01}$)	1.99	1.59	1.32	1
JONSWAP ($z_{1/2}$)	1.26	1.14	1.07	1
JONSWAP (z_1)	1.17	1.09	1.05	1
JONSWAP (z_2)	1.12	1.06	1.03	1
JONSWAP (z_3)	1.11	1.05	1.03	1
DHH ($U_{10}/c_p = 0.83, z_{0.01}$)	2.96	2.06	1.54	1
DHH ($U_{10}/c_p = 4, z_{0.01}$)	3.04	2.19	1.60	1
DHH ($U_{10}/c_p = 0.83, z_{1/2}$)	1.40	1.20	1.10	1
DHH ($U_{10}/c_p = 4, z_{1/2}$)	1.28	1.16	1.08	1
DHH ($U_{10}/c_p = 0.83, z_1$)	1.28	1.14	1.07	1
DHH ($U_{10}/c_p = 4, z_1$)	1.16	1.09	1.05	1
DHH ($U_{10}/c_p = 0.83, z_2$)	1.20	1.10	1.05	1
DHH ($U_{10}/c_p = 4, z_2$)	1.10	1.05	1.02	1
DHH ($U_{10}/c_p = 0.83, z_3$)	1.16	1.08	1.04	1
DHH ($U_{10}/c_p = 4, z_3$)	1.08	1.04	1.02	1
Mono (z_0, z_1, z_2, z_3)	1	1	1	1

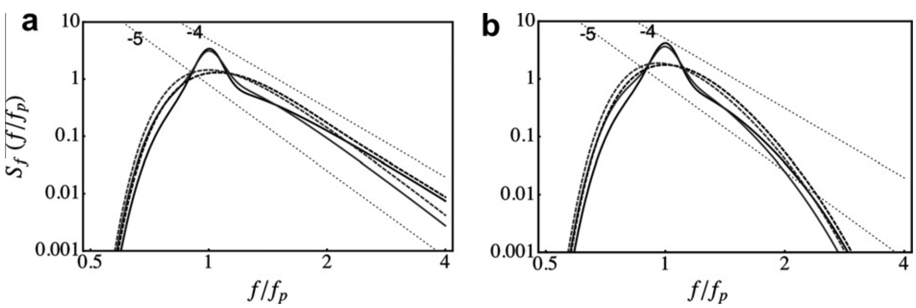

Fig. 1. (a) PM (gray dashed), JONSWAP (gray solid), and DHH spectrum with same peak frequency and significant wave height evaluated near the surface ($z_{0.01}$). The DHH spectrum with wave age 0.83 (black dashed) is rounded, and the DHH spectrum with wave age 4 (black solid) is sharply peaked. (b) Same as (a), but at $z_{1/2}$. Lines proportional to $(f/f_p)^{-4}$ and $(f/f_p)^{-5}$ are also shown (dotted with slope numbers).

by the exponential decay with depth of the higher frequency waves, and thus the spectral shapes are more similar at depth. Because the high-frequency waves decay fastest with depth, it is increasingly inconsequential to the spectrum at depth what spectral slope the high-frequency waves had at the surface.

While the Donelan et al. (1985) DHH spectrum cannot be integrated for Stokes drift at the surface, its Stokes drift behavior at depth is easily integrated and is revealing. In Table 5 for $z_{1/2}$ and deeper, the fully-developed wave age version ($U_{10}/c_p = 0.83$) of the DHH spectrum is nearly identical to the PM spectrum, and the fetch-limited version ($U_{10}/c_p = 4$) is nearly identical to the JONSWAP spectrum. That is, at a moderate depth the shallower tail of the DHH spectrum is no longer affecting the relationships between the moments. However, the $z_{0.01}$ values in Table 5 are quite a bit larger than the PM and JONSWAP spectra, indicating that the shallower tail does play a role near-surface. Consistently, Table 4 shows that the decay with depth of the Stokes drift versus surface moments is substantially faster in the DHH spectrum than in either the PM or JONSWAP cases. Furthermore, all of the realistic spectra tend to approach a monochromatic spectrum with depth, as the higher frequency components of the spectra decay away leaving the waves near the peak frequency.

Note that the b_2 values in Table 4 are particularly useful for the DHH spectrum. They allow estimation of the Stokes drift at depth *even though the Stokes drift and third moment at the surface are not calculable*. This estimation is possible even without additional assumptions, such as truncating the moment estimation or f^{-4} tail of the spectrum at some potentially inaccurate high wavenumber.

If only surface data is available, the most robust approach to reconstructing the subsurface Stokes drift seems to be reconstructing the spectrum parameters α and f_p based on periods (Table 2) or moments (Table 1), and then integrating the spectrum at the appropriate depth. Comparing the JONSWAP results versus the PM in Table 4 gives an indication of how robust these subsurface estimates are likely to be (8–38% subsurface discrepancy shown). Even the DHH spectrum can be used in this manner, although the surface matching must rely on the second moment instead of the indeterminate third moment. Assuming a monochromatic spectrum for the purposes of estimating subsurface Stokes drift is not recommended (factors of 4–7 discrepancy are common).

Harcourt and D'Asaro (2008) argue that, insofar as Langmuir or wave-driven turbulent mixing strength is concerned, that the crucial value is the Stokes drift averaged over the upper 20% of the mixed layer thickness H_{ML}. The rapid decay of empirical spectra by $z_{1/2}$ to very similar moment relationships at depth (Table 5), and thus very similar spectral shapes leads us to consider the nondimensional grouping at $z_{1/2}$, which is $0.8 H_{ML} \pi^2 f_p^2 / g$. If this grouping is substantially greater than one, then the effects from the tail of the empirical spectra will be small, but if this grouping is less than one the tail effects will be important for the strength of Langmuir mixing.

6. Error analysis

The methods above for estimating the Stokes drift magnitude based on different moments of the wave spectrum do not agree wholly between different wave spectral shapes. It is important to consider whether the inaccuracy inherent in using an approximation of the spectral shape is likely to be a larger or smaller error than the known instrumental, modeling, and sampling errors. For this purpose, three datasets are compared, and the discrepancy between them is taken as a measure of uncertainty of Stokes drift measurements generally.

6.1. Description of ERA40 and TOPEX data sets

The WW3 simulation has already been described, and the empirical relationship between $\mathrm{a}_2 D_2$ and surface Stokes drift D_3 are shown in Table 3. The uncertainty in this empirical relationship (e.g., a_2 varies among the spectra by 1.49 to 1.69, or by 12%) is compared to the discrepancy between different wave estimates for the same time period (1994–2001, Tables 7 and 8). When direct Stokes drift data is unavailable, the $\mathrm{a}_2 D_2$ estimate is used as it is the most accurate (Table 6).

The ERA40 reanalysis (Uppala et al., 2005) is a wave and weather data-assimilation using a model that couples an atmospheric model to a wave model (Janssen et al., 2002). This model assimilates the ERS altimeter, including significant wave height, during the time period analyzed, but wave period estimates are constrained only by the wave model physics and wave buoy observations (Caires et al., 2005) which are not common globally. Like WW3, the version of WAM used for ERA40 is a third-generation wave model – both models have similar frequency resolution but ERA40 WAM uses 12 directional bins versus the 24 used for WW3 here. These models differ somewhat in physical parameterizations as well (Ardhuin et al., 2009b).

Table 6
Root-global-mean-square discrepancies using the proposed coefficients for the monochromatic $1\mathrm{D}_h$ surface Stokes drift approximations to the best estimate $U^s = D_{3,WW3}$. The bottom row is normalized by $\sqrt{\langle (U^s)^2\rangle_{G,T}} = 0.182$ m/s.

$\sqrt{\langle (\mathrm{a}_{-1}D_{-1} - U^s)^2\rangle_{G,T}}$	$\sqrt{\langle (\mathrm{a}_1 D_1 - U^s)^2\rangle_{G,T}}$	$\sqrt{\langle (\mathrm{a}_2 D_2 - U^s)^2\rangle_{G,T}}$
0.0522 m/s	0.0342 m/s	0.0196 m/s
0.287	0.188	0.108

The TOPEX/POSEIDON altimeter data is also used to construct a $1\mathrm{D}_h$ Stokes drift estimate independent of a physical wave model for this same period. The significant wave height data is calculated from the standard (Fu et al., 1994) and validated (e.g., Cotton and Carter, 1994; Gower, 1996) method. The Gommenginger et al. (2003) empirical method is used for T_2 wave period and the Gourrion et al. (2002) method for is used for wind speed. Note that this data was not assimilated in ERA40.

One potential difference between these wave products is the wind forcing. Fig. 2a compares the zonal means of the 10-meter wind speeds of the CORE2 wind data used to force the WW3 simulation, the ERA40 reanalysis data, and TOPEX. Although similar, the global wind speeds of the two latter data sets are 6.7–10% lower than the global CORE2 wind speed. The (temporal mean) relative difference between the ERA40 reanalysis and CORE2 data (with respect to CORE2) is shown in Fig. 2b to be as high as 20% in isolated areas. If the interest here were purely a comparison of wave models, then it would be important to use identical winds. However, here an overall uncertainty in Stokes drift is sought, which also depends on the well-known uncertainty in the wind (e.g., Townsend et al., 2000). Since one does not choose the winds for TOPEX, it also has a different forcing than ERA40 and WW3.

Thus, two independent models (with two different wind fields), one data-assimilating and one not, and an empirical altimeter estimate for wave information are available during this period. Using Table 3, all three can be used to generate independent estimates of D_2 (Table 7) and the $1\mathrm{D}_h$ surface Stokes drift magnitude (Table 8). The value $\mathrm{a}_2 = 1.69$ is used for the comparison.

6.2. Comparison and analysis

Fig. 3 compares the mean of the WW3 $1\mathrm{D}_h$ surface Stokes drift magnitude over the aforementioned period (Fig. 3a) to the $\mathrm{a}_2 D_2$ estimate (Fig. 3b). The difference between these fields is modest (Fig. 3c), leading to relatively few areas of percent error greater than 10% (Fig. 3d) and a global mean error under 11% (Table 6). There is structure in the error pattern, as the spectral shape in WW3 differs regionally. For example, some regions may be dominated by simple fully-developed waves where the PM spectrum applies, while other regions may routinely experience superpositions of swell from multiple remote sources leading to a complex spectral shape. The error is largest in the Eastern Pacific, Atlantic, and Indian Oceans – especially in the Southern Hemisphere –

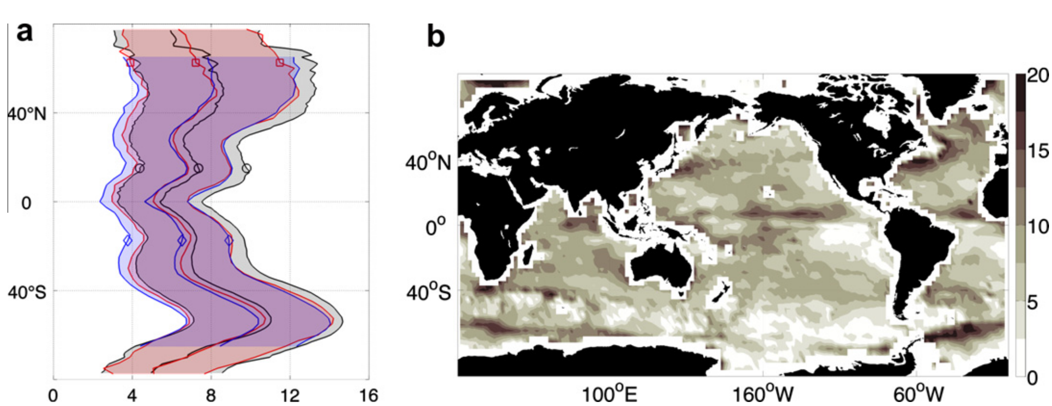

Fig. 2. (a) Comparison of the zonal and temporal mean (1994–2001) of 10-meter wind speed (U_{10}) from ERA40 (red □) and CORE2 (black ∘) reanalyses, and TOPEX satellite data (blue ◇). The shaded interval indicates two-thirds of the distribution centered about the mean. (b) Relative difference between the ERA40 reanalysis and CORE2 U_{10} temporal means using the value 7.71 m/s (the CORE2 temporal and global mean) as reference. (For interpretation of the references to color in this figure legend, the reader is referred to the web version of this article.)

Table 7
Root-global-mean-square discrepancies between the different data sources of D_2 on the reduced ERA40 grid. The bottom row is normalized by $\sqrt{\langle (D_{2,WW3})^2 \rangle_{G,T}} = 0.107$ m/s.

$\sqrt{\langle (D_{2,WW3} - D_{2,ERA})^2 \rangle_{G,T}}$	$\sqrt{\langle (D_{2,WW3} - D_{2,TOP})^2 \rangle_{G,T}}$	$\sqrt{\langle (D_{2,ERA} - D_{2,TOP})^2 \rangle_{G,T}}$
0.0495 m/s	0.0498 m/s	0.0343 m/s
0.463	0.465	0.321

Table 8
Root-global-mean-square discrepancies between the different data sources on the reduced ERA40 grid using the proposed a_2 coefficient for the monochromatic 1D_h surface Stokes drift approximation. The bottom row is normalized by $\sqrt{\langle (D_{3,WW3})^2 \rangle_{G,T}} = 0.182$ m/s.

$\sqrt{\langle (D_{3,WW3} - \mathsf{a}_2 D_{2,ERA})^2 \rangle_{G,T}}$	$\sqrt{\langle (D_{3,WW3} - \mathsf{a}_2 D_{2,TOP})^2 \rangle_{G,T}}$	$\sqrt{\langle (\mathsf{a}_2 D_{2,ERA} - \mathsf{a}_2 D_{2,TOP})^2 \rangle_{G,T}}$
0.0897 m/s	0.0806 m/s	0.0580 m/s
0.493	0.443	0.319

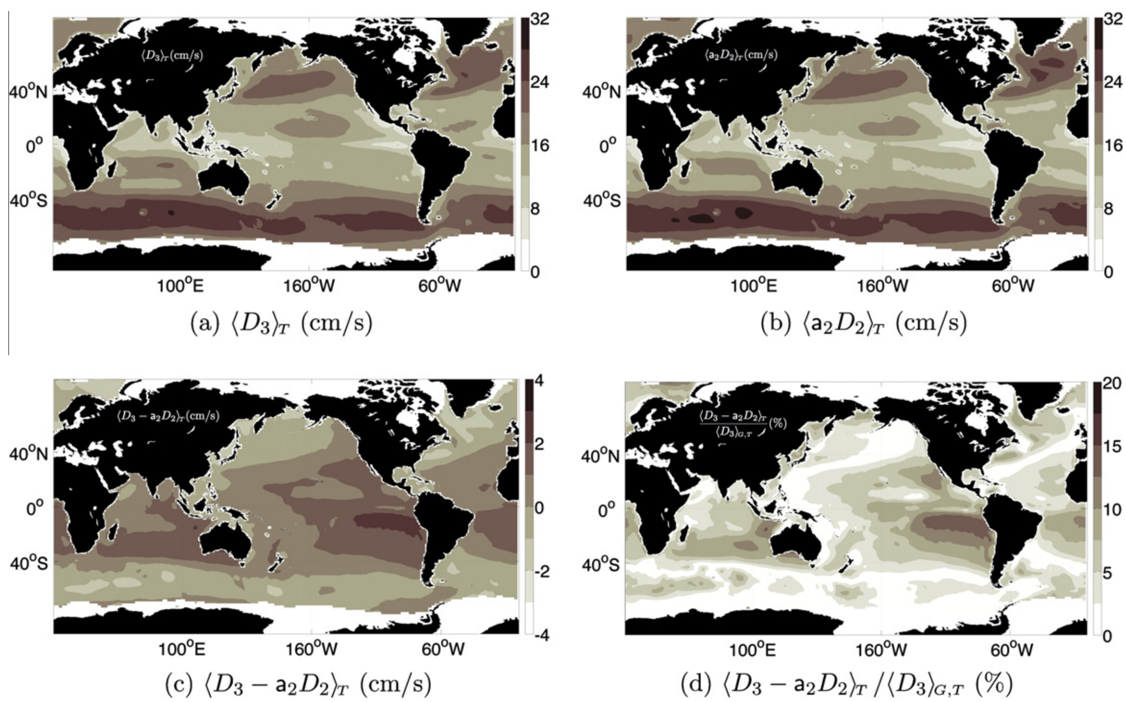

Fig. 3. Eight year mean (1994–2001) of the 1D_h surface Stokes drift magnitude (D_3) compared with the proposed corrected D_2 monochromatic approximation.

which are regions of exceptional wave age (Hanley et al., 2010). In other words, these regions have fewer signatures of fully-developed waves than other regions, which may be due to dominance of swell conditions and variable winds. Thus, it is no surprise that the wave spectrum has a rare shape in these regions.

Fig. 4 makes similar comparisons of Stokes drift magnitude, although this time between ERA40 and WW3 and TOPEX estimates and WW3. Since full spectral information for ERA40 and TOPEX were not available, the $\mathsf{a}_2 D_2$ approximations were used for those datasets, with the value of a_2 determined from WW3. A full spectral estimate of Stokes drift was used for WW3 D_3. It is apparent that the mean and relative mean differences are much larger between the different datasets in Fig. 4 than between the $\mathsf{a}_2 D_2$ estimate and D_3. Regional variations are above 80% where the colorbar is saturated in Fig. 4d and f.

The other estimates for a_2 in Table 3 are smaller than the value of 1.69 used for Fig. 4. However, using a different a_2 estimate is not of much use in reducing the differences in Fig. 4. The ERA40 and TOPEX Stokes drift velocities are generally smaller than WW3, so using the (smaller) values of a_2 found for PM or JONSWAP will only increase these discrepancies. It is, of course, possible to assume a shallower spectral shape for these data products (similar to the DHH spectrum, for example) to increase agreement, but doing so seems arbitrary and likely to result in error cancellations rather than improved accuracy.

Tables 6 and 7 demonstrate that the rgms (root global mean square) discrepancy between U^s and $\mathsf{a}_2 D_{2,WW3}$ (Table 6) is 3–4 times smaller than the rgms discrepancies between the different data products (Table 7). Likewise, the same rgms discrepancy (Table 6) is 4–5 times smaller than the discrepancies in Stokes drift between U^s and $\mathsf{a}_2 D_2$ for ERA40 and TOPEX (Table 8). It is unlikely these large discrepancies (Tables 7 and 8) are due entirely to the differences in wind products alone.

To examine further, consider the derivative (i.e., infinitesimal change in value: ∂) and a finite change in value (Δ) of the natural log of D_2:

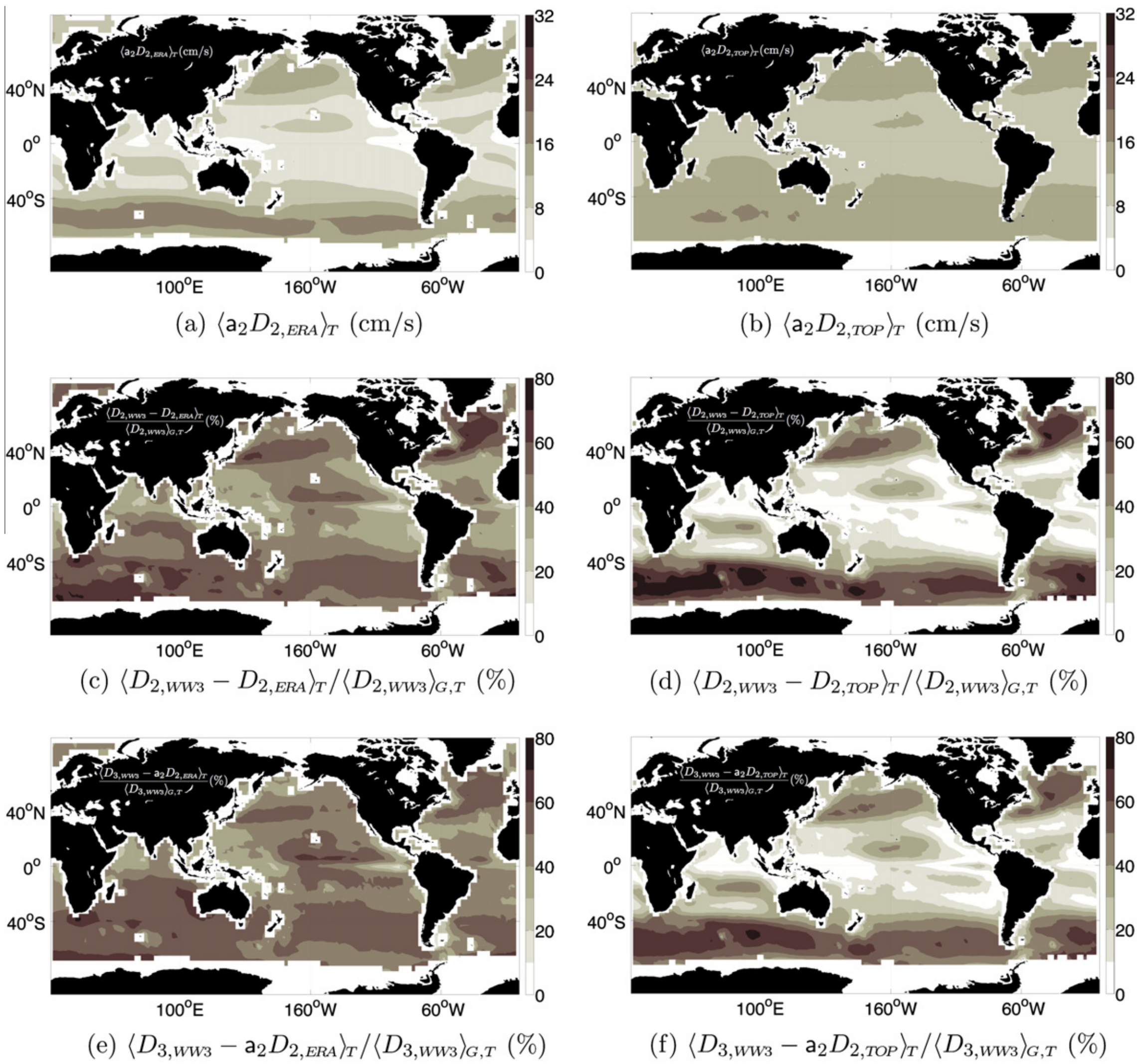

(a) $\langle \mathrm{a}_2 D_{2,ERA} \rangle_T$ (cm/s) (b) $\langle \mathrm{a}_2 D_{2,TOP} \rangle_T$ (cm/s)

(c) $\langle D_{2,WW3} - D_{2,ERA} \rangle_T / \langle D_{2,WW3} \rangle_{G,T}$ (%) (d) $\langle D_{2,WW3} - D_{2,TOP} \rangle_T / \langle D_{2,WW3} \rangle_{G,T}$ (%)

(e) $\langle D_{3,WW3} - \mathrm{a}_2 D_{2,ERA} \rangle_T / \langle D_{3,WW3} \rangle_{G,T}$ (%) (f) $\langle D_{3,WW3} - \mathrm{a}_2 D_{2,TOP} \rangle_T / \langle D_{3,WW3} \rangle_{G,T}$ (%)

Fig. 4. D_2 Comparison of ERA40 reanalysis and TOPEX satellite data with WW3 using eight year means (1994–2001).

$$\partial[\ln(D_2)] = \frac{\partial[D_2]}{D_2} = 2\frac{\partial[H_{m0}]}{H_{m0}} - 3\frac{\partial[T_2]}{T_2}, \tag{47}$$

$$\frac{\Delta D_2}{D_2} \approx 2\frac{\Delta H_{m0}}{H_{m0}} - 3\frac{\Delta T_2}{T_2}. \tag{48}$$

This relationship is useful for propagating the relative changes in H_{m0} and T_2 due to different data to a relative change in D_2. With (48), the D_2 squared difference of WW3 and ERA40 can be approximated as

$$\begin{aligned}
&(D_{2,WW3} - D_{2,ERA})^2 \\
&\approx \left\{ D_{2,WW3}\left[2\frac{(H_{m0,WW3} - H_{m0,ERA})}{H_{m0,WW3}} - 3\frac{(T_{2,WW3} - T_{2,ERA})}{T_{2,WW3}}\right]\right\}^2, \\
&\approx D^2_{2,WW3}\left[4\left(\frac{\Delta H_{m0}}{H_{m0}}\right)^2 + 9\left(\frac{\Delta T_2}{T_2}\right)^2 - 12\frac{\Delta H_{m0}\Delta T_2}{H_{m0}T_2}\right].
\end{aligned} \tag{49}$$

The global mean of (49) yields

$$\frac{\langle (D_{2,WW3} - D_{2,ERA})^2 \rangle_{G,T}}{\langle D^2_{2,WW3} \rangle_{G,T}} = 0.248 + 0.194 + 0.026 = 0.47, \tag{50}$$

where the cross term is the last value in the sum. This approximation is smaller than the actual discrepancy, but it allows a comparison of the factors that contribute. The cross term is small (i.e., the discrepancies are uncorrelated), so the squared discrepancy in D_2 is just

$$\left\langle (D_{2,WW3} - D_{2,ERA})^2 \right\rangle_{G,T} \approx \left\langle D^2_{2,WW3}\left(\frac{2\Delta H_{m0}}{H_{m0}}\right)^2 \right\rangle_{G,T} + \left\langle D^2_{2,WW3}\left(\frac{3\Delta T_2}{T_2}\right)^2 \right\rangle_{G,T} \tag{51}$$

The values in (50) indicate that the contributions from the significant wave height and wave period are of similar magnitude.

$$\left\langle D^2_{2,WW3}\left(\frac{2\Delta H_{m0}}{H_{m0}}\right)^2 \right\rangle_{G,T} \sim \left\langle D^2_{2,WW3}\left(\frac{3\Delta T_2}{T_2}\right)^2 \right\rangle_{G,T} \tag{52}$$

Similarly, the uncertainty in a_2 can be incorporated by beginning with the Stokes drift approximation $\mathrm{a}_2 D_2$.

$$\partial[\ln(\mathrm{a}_2 D_2)] = \frac{\partial[\mathrm{a}_2 D_2]}{\mathrm{a}_2 D_2} \approx \frac{\Delta D_2}{D_2} + \frac{\Delta \mathrm{a}_2}{\mathrm{a}_2}. \tag{53}$$

From Tables 6 and 7 (and that $\mathrm{a}_2 D_2$ is an approximation), we expect the square relative discrepancy between $D_{3,WW3}$ and $\mathrm{a}_2 D_{2,ERA}$ to be larger than between $D_{2,WW3}$ and $D_{2,ERA}$, such that

$$(D_{3,WW3} - \mathsf{a}_2 D_{2,ERA})^2 \gtrapprox \left\{ D_{3,WW3} \left[2\frac{(H_{m0,WW3} - H_{m0,ERA})}{H_{m0,WW3}} - 3\frac{(T_{2,WW3} - T_{2,ERA})}{T_{2,WW3}} + \frac{\Delta \mathsf{a}_2}{\mathsf{a}_2} \right] \right\}^2. \quad (54)$$

In addition, under the assumption that errors in a_2 and D_2 are uncorrelated, it follows that the global mean can be bounded as

$$\frac{\langle (D_{3,WW3} - \mathsf{a}_2 D_{2,ERA})^2 \rangle_{G,T}}{\langle D^2_{3,WW3} \rangle_{G,T}} \gtrapprox 0.245 + 0.218 + \left\langle \left(\frac{\Delta \mathsf{a}_2}{\mathsf{a}_2} \right)^2 \right\rangle + \langle \text{c.t.} \rangle. \quad (55)$$

Suppose the spectral shape is assumed to be the primary cause of the error in the Stokes drift approximation. Then the 12% spread of a_2 among the different spectral shapes in Table 3 is a good approximation of $\Delta \mathsf{a}_2/\mathsf{a}_2$ in (55). Inserting, we find that

$$\langle (D_{3,WW3} - \mathsf{a}_2 D_{2,ERA})^2 \rangle_{G,T} \gtrapprox 0.245 + 0.218 + 0.014 + \langle \text{c.t.} \rangle, \quad (56)$$

which implies $\Delta \mathsf{a}_2/\mathsf{a}_2 \ll \Delta D_2/D_2$.

A similar approach can be used to analyze the discrepancies due to the differences in wind products. Modifying (25), the PM $1D_h$ surface Stokes drift can be rewritten to account for non-fully-developed wave conditions. Let $U^s_{PM'} \equiv \mu_c U^s_{PM'}$, where μ_c is some unknown non-zero function providing the change to Stokes drift due to a lack of full development. For example, the JONSWAP spectrum has a combination of fetch and windspeed playing a similar role to μ_c in (32). Then the approximation of the derivative of the natural log of $U^s_{PM'}$ yields

$$\frac{\Delta U^s_{PM'}}{U^s_{PM'}} = \frac{\Delta U^s_{PM}}{U^s_{PM}} + \frac{\Delta \mu_c}{\mu_c} = \frac{\Delta U_{10}}{U_{10}} + \frac{\Delta \mu_c}{\mu_c}. \quad (57)$$

Assuming ΔU_{10} and $\Delta \mu_c$ are uncorrelated, the first order, relative U_{10} gms difference between WW3 and ERA40 yields

$$\frac{\left\langle \left(U^s_{PM,ERA} - U^s_{PM,WW3} \right)^2 \right\rangle}{\left\langle \left(U^s_{PM,WW3} \right)^2 \right\rangle} = \frac{\langle (U_{10,ERA} - U_{10,WW3})^2 \rangle}{\langle (U_{10,WW3})^2 \rangle} = 0.047. \quad (58)$$

Since (58) accounts for only one fifth of the square of the ERA40 to WW3 discrepancy found in Table 8, the different winds being used is not enough to explain the difference in Stokes drift. Similarly, the difference in ERA40 and TOPEX winds is not enough to explain the difference in Stokes drift.

In summary, estimates of Stokes drift from different data products disagree by 30–50%, which is roughly equally divided between discrepancies in significant wave height and wave period. The error in approximating the $1D_h$ Stokes drift as $\mathsf{a}_2 D_2$ can be approximated to be 12% from the range of a_2 values from all the spectral shapes examined here. Another estimate of 11% from directly comparing $\mathsf{a}_2 D_2$ and D_3 in WW3 is smaller. These errors would need to be four times larger to rival the contributions from the significant wave height and period discrepancies. Furthermore, the traditional assumption that Stokes drift can be approximated by assuming fully-developed waves as in (25), (32), and McWilliams and Restrepo (1999), underestimates the Stokes drift discrepancies found here by 40–125%. We hypothesize that the reason is the lack of full development globally (Hanley et al., 2010).

7. Summary and conclusion

By comparing the integrals of spectra from WW3, JONSWAP, DHH, and PM, relationships between different moments of the spectra, period estimates, and Stokes drift have been found and tabulated. The reliability of these relationships may be judged both by comparison between the spectral shapes and by comparison to the discrepancies between available wave data products.

It is found that the most reliable estimator of Stokes drift is found from the third moment of the wave spectrum, but an estimate based on the second moment is usually quite accurate away from coastal areas. At depth, all wave spectra can have their first through third moments estimated, and the relationship between these moments becomes increasingly consistent between the different spectra. Estimating subsurface Stokes drift by this method requires care, but is feasible. The third moment is not calculable for some empirical spectral shapes at the surface without additional assumptions, so being able to use the second or lower moments at the surface to determine Stokes drift at depth is quite useful.

Based on the arguments presented up to this point, an accurate and full reconstruction of wave spectrum is required to fully diagnose Stokes drift. This is possible at some buoy locations, but not globally and care is needed (see Appendix A.5). The ERA40 dataset assimilates some data, but is lacking in resolution and some parameterizations required for accurate modeling of Stokes drift (Ardhuin et al., 2009b). The altimeter dataset used here is a measurement of sort, but relies heavily on empirical relationships that are as likely to fail as the theoretical spectral results presented here. The approach taken by McWilliams and Restrepo (1999) is also shown here to be unreliable, as the assumption of fully-developed waves is estimated to cause nearly as much bias as any of the other estimates. In summary, there is presently no well-accepted way to determine the global Stokes drift and it is the intention of the authors that the results of this paper may help to compare and refine present data sources until a reliable global dataset is produced.

The wave models used here are driven with different wind products, to allow for variations in common wind products to play a role in the Stokes drift estimates. If the goal here were to contrast the Stokes drift from two different wave models, the same winds would be used to force both. However, a detailed model bias comparison was not the goal here, and these comparisons can be found elsewhere (e.g., Hanson et al., 2009). It was the goal here to use three substantially different estimates of Stokes drift, from satellites, a data-assimilating model, and a forward model, to see how reasonable estimates of Stokes drift differ.

As collection and analysis of wave data becomes more sophisticated, it is increasingly important to compare different datasets. The tables and analysis presented here are intended to aid in this process and to guide the collection of data as well. For example, retaining the third moment of the wave spectrum in addition to significant wave height and mean or zero-crossing wave period in data would greatly increase the accuracy of our determination of the global climatology and variability of Stokes drift.

Acknowledgement

This work was supported by NASA ROSES-NNX09AF38G and NSF OCE-0934737. Data preparation by Benjamin Hamlington and Erik Baldwin-Stevens is gratefully acknowledged. Discussions on drafts of the paper with Ramsey Harcourt, Eric D'Asaro, and Luke Van Roekel proved invaluable.

Appendix A. Derivation of a wave-averaged Stokes drift velocity

A.1. Stokes drift velocity

The Stokes drift velocity (throughout as Stokes drift) may be defined in a number of ways. Generally, the Stokes drift is the mean difference between the Lagrangian velocity $\boldsymbol{u}^L$ (the velocity following the motion of a fluid parcel) and the Eulerian velocity $\boldsymbol{u}^E$. We will define the Stokes drift as a time and spatial average over a period $T \neq 0$ (since the instantaneous value of these velocities is identical at a given location) and a horizontal length scale $\boldsymbol{X}_h = (X_h, Y_h)$ (to remove high frequency variations). Let the position of a fluid parcel at time t be given by $\boldsymbol{x}_p(t)$. Here the interest is estimating the basic wave-averaged dynamics as set out by Craik and Leibovich (1976) and McWilliams and Restrepo (1999), without higher-order effects. Then the Lagrangian and Eulerian velocities and fluid parcel displacements can be related through the same Taylor-series expansions:

$$\boldsymbol{u}^L(\boldsymbol{x}_p(t_0), t) = \boldsymbol{u}^E(\boldsymbol{x}_p(t), t), \tag{A.1}$$

$$\boldsymbol{u}^L(\boldsymbol{x}_p(t_0), t) = \boldsymbol{u}^E(\boldsymbol{x}_p(t_0), t) + (\boldsymbol{x}_p(t) - \boldsymbol{x}_p(t_0)) \cdot \nabla \boldsymbol{u}^E(\boldsymbol{x}_p(t), t)\big|_{\boldsymbol{x}_p(t_0)} + \cdots, \tag{A.2}$$

$$\begin{aligned}\boldsymbol{x}_p(t) - \boldsymbol{x}_p(t_0) &= \int_{t_0}^{t} \boldsymbol{u}^L(\boldsymbol{x}_p(t_0), s')ds' \\ &= \int_{t_0}^{t} (\boldsymbol{u}^E(\boldsymbol{x}_p(t_0), s') + \cdots)ds'.\end{aligned} \tag{A.3}$$

As previously mentioned, we will formally define the Stokes drift as

$$\boldsymbol{u}^S(\boldsymbol{x}, t; \boldsymbol{X}_h, T) \equiv \langle \boldsymbol{u}^L(\boldsymbol{x}, t) - \boldsymbol{u}^E(\boldsymbol{x}, t)\rangle_{\boldsymbol{X}_h, T} \tag{A.4}$$

$$\equiv \frac{1}{T}\int_{t-T/2}^{t+T/2} \langle \boldsymbol{u}^L(\boldsymbol{x}, s) - \boldsymbol{u}^E(\boldsymbol{x}, s)\rangle_{\boldsymbol{X}_h} ds \tag{A.5}$$

$$\equiv \frac{1}{X_h Y_h}\int_{\boldsymbol{x}_h-\boldsymbol{X}_h/2}^{\boldsymbol{x}_h+\boldsymbol{X}_h/2} \langle \boldsymbol{u}^L(\boldsymbol{x}'_h, z, s) - \boldsymbol{u}^E(\boldsymbol{x}'_h, z, s)\rangle_T d\boldsymbol{x}'_h, \tag{A.6}$$

where angle brackets denote time or spatial averaging and are defined throughout as in (A.5) and (A.6). Substitutions then yield the lowest-order estimate:

$$\begin{aligned}&\langle \boldsymbol{u}^L(\boldsymbol{x}_p(t_0), t_0) - \boldsymbol{u}^E(\boldsymbol{x}_p(t_0), t_0)\rangle_T \\ &\approx \frac{1}{T}\int_{t_0-T/2}^{t_0+T/2} (\boldsymbol{x}_p(t) - \boldsymbol{x}_p(t_0)) \cdot \nabla \boldsymbol{u}^E(\boldsymbol{x}_p(t), t)\Big|_{\boldsymbol{x}_p(t_0)} dt \qquad (A.7) \\ &\approx \frac{1}{T}\int_{t_0-T/2}^{t_0+T/2} \left(\int_{t_0}^{t} \boldsymbol{u}^E(\boldsymbol{x}_p(t_0), s')ds'\right) \cdot \nabla \boldsymbol{u}^E(\boldsymbol{x}_p(t), t)\Big|_{\boldsymbol{x}_p(t_0)} dt, \qquad (A.8)\end{aligned}$$

$$\boldsymbol{u}^S(\boldsymbol{x}, t; \boldsymbol{X}_h, T) \approx \left\langle \frac{1}{T}\int_{t-T/2}^{t+T/2} \left(\int_{t}^{s} \boldsymbol{u}^{\mathrm{w}}(\boldsymbol{x}, s')ds'\right) \cdot \nabla \boldsymbol{u}^{\mathrm{w}}(\boldsymbol{x}, s)ds \right\rangle_{\boldsymbol{X}_h}. \tag{A.9}$$

It should be emphasized that the interval T is sufficient to average over relevant wave displacements by the fast wave velocity $\boldsymbol{u}^{\mathrm{w}}$, but not so long that Stokes drift is not a function of time, for example due to wind variability. Similarly, the horizontal length scale $\boldsymbol{X}_h$ is sufficient to remove high frequency fluctuations but not long enough to smooth the frequencies of interest. This smoothing is essential for Stokes drift since it removes possible spatially-oscillatory waves that are independent of time (see Appendix A.5 for an example).

Stokes drift, as defined, appears often in the wave-averaged dynamics, e.g., in transporting tracers, and is closely related to the vortex force related to Langmuir turbulence (Craik and Leibovich, 1976; McWilliams et al., 1997), the mass transport by waves, the wave-related pressure, and the wave surface stress correction (McWilliams and Restrepo, 1999). Any one of these quantities may be of interest for inclusion in large-scale ocean modeling.

A.2. Derivation of Stokes drift in wave spectral density form

Previous derivations of the full (three dimensional) Stokes drift in wave spectral density form can be found in Kenyon (1969) and McWilliams and Restrepo (1999). To further illustrate, a spectral density estimate for use in a wave model is presented.

A.2.1. Wave field decomposition for model inclusion

To illustrate concretely, consider a spectral linear wave model with an arbitrary domain $\boldsymbol{L}_h$ consisting of grid cells $L \times L$ in size. Furthermore, assume that the wave dynamics being modeled are separable into fast and slow scales, such that the fast dynamics can be represented within each grid cell by a periodic, statistically homogeneous and stationary wave field. Then the slower dynamics can be represented by mean properties of each cell that vary slowly from neighbor to neighbor. For purposes of this derivation, a series approximation will be used to represent the fast dynamics while cell grid averages will serve to model the slower ones.

Now within each grid cell, let an arbitrary wave field with a surface displacement η be approximated by a superposition of solutions to the linear water wave equation. Since wave velocities are irrotational to leading order, they may be expressed by a velocity potential φ and the classical solutions are readily derived:

$$\boldsymbol{u}^{\mathrm{w}} = (\boldsymbol{u}_h^{\mathrm{w}}, w^{\mathrm{w}}) = -\nabla\varphi^{\mathrm{w}}, \tag{A.10}$$

$$\varphi_{\mathbf{k}}^{\mathrm{w}} = -\frac{e^{kz}}{k}\frac{\partial \eta_{\mathbf{k}}^{\mathrm{w}}(\boldsymbol{x}_h, t)}{\partial t}, \tag{A.11}$$

$$\eta_{\mathbf{k}}^{\mathrm{w}} = a_{\mathbf{k}} \cos\left[\mathbf{k}\cdot\boldsymbol{x}_h - \omega_{\mathbf{k}}^{+} t + \tau_{\mathbf{k}}\right]. \tag{A.12}$$

Here, $\eta_{\mathbf{k}}^{\mathrm{w}}$, for a given horizontal wavevector $\mathbf{k}$ (and wavenumber $k = |\mathbf{k}|$), has amplitude $a_{\mathbf{k}}$ (slowly varying in space and time), phase shift $\tau_{\mathbf{k}}$, and positive frequency $\omega_{\mathbf{k}}^{+} = \omega_k^{+} = \sqrt{gk}$. These solutions and dispersion relation are appropriate if small wave slope ($ka_{\mathbf{k}} \ll 1$) and deep water ($kD \gg 1$) are assumed. If in addition, the linear solutions are periodic at the boundary, $\eta_{\mathbf{k}}^{\mathrm{w}}$ has discrete wavevectors ($\mathbf{k} = \mathbf{k}_{m,n} = (k_{x_m}, k_{y_n}) = \frac{2\pi}{L}(m, n)$, for $m, n = 0, \pm1, \pm2, \ldots$) and can be reformulated as

$$\eta_{\mathbf{k}_{mn}}^{\mathrm{w}} = c_{\mathbf{k}_{mn}} e^{i[\mathbf{k}_{mn}\cdot\boldsymbol{x}_h - \omega_{\mathbf{k}_{mn}} t]} + c_{\mathbf{k}_{mn}}^{*} e^{-i[\mathbf{k}_{mn}\cdot\boldsymbol{x}_h - \omega_{\mathbf{k}_{mn}} t]}, \tag{A.13}$$

where $c_{\mathbf{k}_{mn}}$ corresponds to $\frac{1}{2}a_{\mathbf{k}_{mn}}e^{i\tau_{\mathbf{k}_{mn}}}$. For further simplicity, assume that the grid cell is centered at the origin and η, $\frac{\partial}{\partial t}\eta$ are known at time $t = 0$. Also let all m, n subscripts be implied. Then the approximated surface displacement η^{w} may be rewritten as a finite superposition of linear solutions (discretized in the wavevector domain) with readily determined Fourier coefficients:

$$\eta \approx \eta^{\mathrm{w}}(\boldsymbol{x}_h, t) = \sum_{m,n=-N}^{N} c_{\mathbf{k}} e^{i[\mathbf{k}\cdot\boldsymbol{x}_h - \omega_{\mathbf{k}} t]} + c_{\mathbf{k}}^{*} e^{-i[\mathbf{k}\cdot\boldsymbol{x}_h - \omega_{\mathbf{k}} t]}, \tag{A.14}$$

$$\Re\{c_{\mathbf{k}}\} = \frac{1}{2}(c_{\mathbf{k}} + c_{\mathbf{k}}^{*}) = \frac{1}{2L^2}\int_{-\boldsymbol{L}_h/2}^{\boldsymbol{L}_h/2} \eta(\boldsymbol{x}_h, 0)e^{-i[\mathbf{k}\cdot\boldsymbol{x}_h]} d\boldsymbol{x}_h, \tag{A.15}$$

$$\Im\{c_{\mathbf{k}}\} = \frac{1}{2i}(c_{\mathbf{k}} - c_{\mathbf{k}}^{*}) = \frac{1}{2L^2}\int_{-\boldsymbol{L}_h/2}^{\boldsymbol{L}_h/2} \frac{1}{\omega_{\mathbf{k}}}\frac{\partial \eta(\boldsymbol{x}_h, 0)}{\partial t} e^{-i[\mathbf{k}\cdot\boldsymbol{x}_h]} d\boldsymbol{x}_h. \tag{A.16}$$

It then follows that $a_{\mathbf{k}} = 2|c_{\mathbf{k}}|$, $\tau_{\mathbf{k}} = arg(c_{\mathbf{k}})$, and $\langle \eta^{\mathrm{w}}(\boldsymbol{x}_h, t)\rangle_{\boldsymbol{L}_h} = 0$ (since $\eta_{\mathbf{k}}^{\mathrm{w}}$ is horizontally harmonic). It should be noted though that the surface displacement is not a Fourier series in time due to the dispersion relation and in general, $\langle \eta^{\mathrm{w}}(\boldsymbol{x}_{0_h}, t)\rangle_T \neq 0$ for any fixed point $\boldsymbol{x}_{0_h}$ and arbitrary T since

$$\langle \eta^{\mathrm{w}}(\boldsymbol{x}_{0_h}, t)\rangle_T = \frac{1}{T}\int_{t-T/2}^{t+T/2} \eta^{\mathrm{w}}(\boldsymbol{x}_{0_h}, s)\,dt \tag{A.17}$$

$$= \frac{1}{T}\int_{t-T/2}^{t+T/2} \left\{\sum_{m,n=-N}^{N} \left(c_{\mathbf{k}} e^{i[\mathbf{k}\cdot\boldsymbol{x}_{0_h} - \omega_{\mathbf{k}} s]} + \text{c.c.}\right)\right\} ds \tag{A.18}$$

$$= \sum_{m,n=-N}^{N} 2\Re\{d_{\mathbf{k}}(t)\}\frac{\sin(T\omega_{\mathbf{k}}/2)}{T\omega_{\mathbf{k}}/2}, \tag{A.19}$$

where $d_{\mathbf{k}}(t) = c_{\mathbf{k}} e^{i[\mathbf{k}\cdot\boldsymbol{x}_{0_h} - \omega_{\mathbf{k}} t]}$ and c.c. denotes the complex conjugate. Although η^{w} is defined deterministically, it can be thought of as a statistically stationary process (in the wide-sense) since the expected (the large limit) mean (for time) is constant ($E\{\eta^{w}\}=0$) and the autocorrelation function (for time) is only dependent on one variable ($R(t_1,t_2)=R(t)$ for $t=t_1-t_2$). To minimize error in this first order approximation, it will be assumed $T \gg \sqrt{2L/\pi g}$ throughout.

Lastly, to sufficiently model wind and swell conditions (for Stokes drift), L needs to be on the order of 1 km or greater. On a typical $1^\circ \times 1.25^\circ$ latitude-longitude grid, the dimensions of the grid range approximately from 110×140 km (at the equator) to 110×35 km (75° latitude). Capillary waves can be excluded in the summation by ensuring the smallest wavelength is approximately 10 cm, equivalent to $N = O(10^4 L)$ (per km).

A.2.2. Wave spectral density estimates

For statistically homogeneous and stationary waves, there is a direct relationship between the expected wave variance (the height deviation squared) and the Fourier transform of the height deviation, magnitude squared, in the frequency and wavevector domain. This latter part is often referred to as the spectral density and can be derived using a modified form of Plancherel's theorem. For simplification, consider the 1D time–frequency relationship for some point $\boldsymbol{x}_{0_h}$ where the surface displacement is ignored outside an interval of length T. Let

$$\eta_T(t) = \begin{cases} \eta(\boldsymbol{x}_{0_h}, t), & |t| \leqslant T, \\ 0, & |t| > T, \end{cases} \tag{A.20}$$

$$\mathcal{F}[\eta_T](\omega) = \frac{1}{\sqrt{2\pi}} \int_{-\infty}^{\infty} \eta_T(t) e^{-i\omega t} dt. \tag{A.21}$$

Then Plancherel's theorem can be used for piecewise continuous η-whether or not it is absolutely and quadratically integrable[11]-to establish a relationship between the variance of (A.20) and the magnitude square of (A.21). Taking limits, a general spectral density $\mathcal{S}$ can be defined as

$$\lim_{T\to\infty} \frac{1}{T} \int_{-\infty}^{\infty} |\eta_T(s)|^2 ds = \lim_{T\to\infty} \frac{1}{T} \int_{-\infty}^{\infty} |\mathcal{F}[\eta_T](\omega)|^2 d\omega = \int_{-\infty}^{\infty} \mathcal{S}(\omega) d\omega. \tag{A.22}$$

If η is statistically stationary (as previously defined), it can be shown that

$$\lim_{T\to\infty} \frac{1}{T} |\mathcal{F}[\eta_T](\omega)|^2 = \mathcal{S}(\omega), \tag{A.23}$$

and a discrete frequency form of (A.22) follows

$$\lim_{\Delta\omega\to 0} \sum_{j=-\infty}^{\infty} \left(\lim_{T\to\infty} \frac{|\mathcal{F}_j[\eta_T^{w}]|^2}{T} \right) \Delta\omega_j = \lim_{\Delta\omega\to 0} \sum_{j=-\infty}^{\infty} \mathcal{S}_j^{w} \Delta\omega_j, \tag{A.24}$$

where $\mathcal{F}_j$ denotes the Fourier transform for a discrete frequency ω_j of η_T^{w}.

Similarly, a relationship can be derived for the entire domain utilizing the deep–water dispersion relation (and noting η is real):

$$\lim_{T,L\to\infty} \langle \eta(\boldsymbol{x}_h, t)^2 \rangle_{T,\boldsymbol{L}_h} \equiv \int \int_{-\infty}^{\infty} G(\mathbf{k}, \omega)\, d\mathbf{k} d\omega \equiv \int_{-\infty}^{\infty} \mathcal{S}_{\mathbf{k}}(\mathbf{k})\, d\mathbf{k}, \tag{A.25}$$

where[11]

$$\mathcal{S}_{\mathbf{k}}(\mathbf{k}) = 2 \int_0^{\infty} \delta(\omega - \sqrt{gk}) G(\mathbf{k}, \omega)\, d\omega. \tag{A.26}$$

[11] The use of η_T ensures the Fourier transform exists and (A.20) and (A.21) are quadratically integrable.

Using (A.25), a spectral density estimate now can be defined in the large T and L approach. First note that

$$\int_{-\boldsymbol{L}_h/2}^{\boldsymbol{L}_h/2} \eta^{w}(\boldsymbol{x}_h, s)^2 d\boldsymbol{x}$$

$$= \int_{-\boldsymbol{L}_h/2}^{\boldsymbol{L}_h/2} \left(\sum_{m,n=-N}^{N} c_{\mathbf{k}} e^{i[\mathbf{k}\cdot\boldsymbol{x}_h - \omega_{\mathbf{k}} s]} + c_{\mathbf{k}}^{*} e^{-i[\mathbf{k}\cdot\boldsymbol{x}_h - \omega_{\mathbf{k}} s]} \right)^2 d\boldsymbol{x} \tag{A.27}$$

$$= \sum_{m,n,\grave{m},\grave{n}=-N}^{N} \Bigg[\int_{-\boldsymbol{L}_h/2}^{\boldsymbol{L}_h/2} \Big(c_{\mathbf{k}} \grave{c}_{\mathbf{k}} e^{i[(\mathbf{k}+\grave{\mathbf{k}})\cdot\boldsymbol{x}_h - (\omega_{\mathbf{k}}+\omega_{\grave{\mathbf{k}}})s]} + c_{\mathbf{k}} \grave{c}_{\mathbf{k}}^{*} e^{i[(\mathbf{k}-\grave{\mathbf{k}})\cdot\boldsymbol{x}_h - (\omega_{\mathbf{k}}-\omega_{\grave{\mathbf{k}}})s]} + c_{\mathbf{k}}^{*} \grave{c}_{\mathbf{k}} e^{-i[(\mathbf{k}-\grave{\mathbf{k}})\cdot\boldsymbol{x}_h - (\omega_{\mathbf{k}}-\omega_{\grave{\mathbf{k}}})s]} + c_{\mathbf{k}}^{*} \grave{c}_{\mathbf{k}}^{*} e^{-i[(\mathbf{k}+\grave{\mathbf{k}})\cdot\boldsymbol{x}_h - (\omega_{\mathbf{k}}+\omega_{\grave{\mathbf{k}}})s]} \Big) d\boldsymbol{x} \Bigg] \tag{A.28}$$

$$= \sum_{m,n=-N}^{N} L^2 \left(2 c_{\mathbf{k}} c_{\mathbf{k}}^{*} + c_{\mathbf{k}} c_{-\mathbf{k}} e^{-i2\omega_{\mathbf{k}} s} + c_{\mathbf{k}}^{*} c_{-\mathbf{k}}^{*} e^{i2\omega_{\mathbf{k}} s} \right), \tag{A.29}$$

and

$$\frac{1}{TL^2} \int_{t-\frac{T}{2}}^{t+\frac{T}{2}} \int_{-\boldsymbol{L}_h/2}^{\boldsymbol{L}_h/2} \eta^{w}(\boldsymbol{x}_h, s)^2 d\boldsymbol{x} ds$$

$$= \sum_{m,n=-N}^{N} 2 c_{\mathbf{k}} c_{\mathbf{k}}^{*} + \frac{\sin(T\omega_{\mathbf{k}})}{T\omega_{\mathbf{k}}} \left(c_{\mathbf{k}} c_{-\mathbf{k}} e^{-i2\omega_{\mathbf{k}} t} + c_{\mathbf{k}}^{*} c_{-\mathbf{k}}^{*} e^{i2\omega_{\mathbf{k}} t} \right) \tag{A.30}$$

$$= \sum_{m,n=-N}^{N} 2 c_{\mathbf{k}} c_{\mathbf{k}}^{*} \left[1 + \frac{\sin(T\omega_{\mathbf{k}})}{T\omega_{\mathbf{k}}} \cos(2\omega_{\mathbf{k}} t) \right]. \tag{A.31}$$

It then follows for T sufficiently large, the spectral density of the surface displacement η can be approximated as a sum of Fourier coefficients of a linear approximation, or

$$\int_{-\infty}^{\infty} \mathcal{S}_{\mathbf{k}}(\mathbf{k}) d\mathbf{k} \approx \lim_{T,L\to\infty} \langle \eta^{w}(\boldsymbol{x}_h, t)^2 \rangle_{T,\boldsymbol{L}_h} \approx \sum_{m,n=-N}^{N} 2 c_{\mathbf{k}} c_{\mathbf{k}}^{*}. \tag{A.32}$$

A.2.3. The Stokes drift cell-average estimate

With η in series form, the other series for wave variables and desired forms formally follow:

$$\varphi^{w}(\boldsymbol{x}, t) = \sum_{m,n=-N}^{N} \frac{i c_{\mathbf{k}} \omega_{\mathbf{k}}}{k} e^{kz + i[\mathbf{k}\cdot\boldsymbol{x}_h - \omega_{\mathbf{k}} t]} + c.c., \tag{A.33}$$

$$\boldsymbol{u}^{w}(\boldsymbol{x}, t) = \sum_{m,n=-N}^{N} (k_x, k_y, -ik) \frac{c_{\mathbf{k}} \omega_{\mathbf{k}}}{k} e^{kz + i[\mathbf{k}\cdot\boldsymbol{x}_h - \omega_{\mathbf{k}} t]} + c.c., \tag{A.34}$$

$$\nabla \boldsymbol{u}^{w}(\boldsymbol{x}, t) = \sum_{m,n=-N}^{N} (k_x, k_y, -ik) \otimes (ik_x, ik_y, k) \times \frac{c_{\mathbf{k}} \omega_{\mathbf{k}}}{k} e^{kz + i[\mathbf{k}\cdot\boldsymbol{x}_h - \omega_{\mathbf{k}} t]} + c.c., \tag{A.35}$$

$$\int_t^s \boldsymbol{u}^{w}(\boldsymbol{x}, s') ds' = \sum_{m,n=-N}^{N} (ik_x, ik_y, k) \frac{c_{\mathbf{k}}}{k} e^{kz + i[\mathbf{k}\cdot\boldsymbol{x}_h]} (e^{-i\omega_{\mathbf{k}} s} - e^{-i\omega_{\mathbf{k}} t}) + c.c.. \tag{A.36}$$

Here, the outer product $\otimes$ emphasizes the tensor rank of $\nabla \boldsymbol{u}^{w}(\boldsymbol{x}, t)$. It then follows that the difference between the Eulerian and Lagrangian velocities at time s for some fixed initial t is

$$\left(\int_t^s \boldsymbol{u}^{\mathrm{w}}(\boldsymbol{x},s')ds'\right)\cdot\nabla\boldsymbol{u}^{\mathrm{w}}(\boldsymbol{x},s)$$
$$=\left\{\left[\sum_{m,n=-N}^{N}(ik_x,ik_y,k)\frac{c_{\mathbf{k}}}{k}e^{kz+i[\mathbf{k}\cdot\boldsymbol{x}_h]}(e^{-i\omega_{\mathbf{k}}s}-e^{-i\omega_{\mathbf{k}}t})+c.c.\right]\right.$$
$$\cdot\left[\sum_{m',n'=-N}^{N}(\grave{k}_x,\grave{k}_y,-i\grave{k})\otimes(i\grave{k}_x,i\grave{k}_y,\grave{k})\frac{\grave{c}_{\mathbf{k}}\grave{\omega}_{\mathbf{k}}}{\grave{k}}e^{\grave{k}z+i[\grave{\mathbf{k}}\cdot\boldsymbol{x}_h-\grave{\omega}_{\mathbf{k}}s]}\right.$$
$$\left.\left.+c.c.\right]\right\} \tag{A.37}$$
$$=\sum_{m,n,m',n'=-N}^{N}\left\{(\grave{k}_x,\grave{k}_y,-i\grave{k})\frac{\grave{c}_{\mathbf{k}}\grave{\omega}_{\mathbf{k}}}{k\grave{k}}e^{(k+\grave{k})z}\right.$$
$$\times\left[(-k_x\grave{k}_x-k_y\grave{k}_y+\grave{k}k)c_{\mathbf{k}}e^{i[(\mathbf{k}+\grave{\mathbf{k}})\cdot\boldsymbol{x}_h]}(e^{-i[(\omega_{\mathbf{k}}+\grave{\omega}_{\mathbf{k}})s]}-e^{-i[\omega_{\mathbf{k}}t+\grave{\omega}_{\mathbf{k}}s]})\right.$$
$$\left.\left.+(k_x\grave{k}_x+k_y\grave{k}_y+k\grave{k})c^*_{\mathbf{k}}e^{-i[(\mathbf{k}-\grave{\mathbf{k}})\cdot\boldsymbol{x}_h]}(e^{i[(\omega_{\mathbf{k}}-\grave{\omega}_{\mathbf{k}})s]}-e^{i[\omega_{\mathbf{k}}t-\grave{\omega}_{\mathbf{k}}s]})\right]+c.c.\right\}. \tag{A.38}$$

The spatial average of the difference over the periodic domain gives

$$\frac{1}{L^2}\int_{-\boldsymbol{L}_h/2}^{\boldsymbol{L}_h/2}\left[\left(\int_t^s\boldsymbol{u}^{\mathrm{w}}(\boldsymbol{x},s')ds'\right)\cdot\nabla\boldsymbol{u}^{\mathrm{w}}(\boldsymbol{x},s)\right]d\boldsymbol{x}_h$$
$$=\sum_{m,n=-N}^{N}\{(k_x,k_y,ik)2c_{\mathbf{k}}c_{-\mathbf{k}}\omega_{\mathbf{k}}e^{2kz}(e^{-i[\omega_{\mathbf{k}}(t+s)]}-e^{-i2\omega_{\mathbf{k}}s})$$
$$+(k_x,k_y,-ik)2c^*_{\mathbf{k}}c_{\mathbf{k}}\omega_{\mathbf{k}}e^{2kz}(1-e^{i[\omega_{\mathbf{k}}(t-s)]})\}+c.c.. \tag{A.39}$$

Similarly, integrating in time over the interval $[t-T/2, t+T/2]$, we find

$$\frac{1}{T}\int_{t-T/2}^{t+T/2}\left\{\frac{1}{L^2}\int_{-\boldsymbol{L}_h/2}^{\boldsymbol{L}_h/2}\left[\left(\int_t^s\boldsymbol{u}^{\mathrm{w}}(\boldsymbol{x},s')ds'\right)\cdot\nabla\boldsymbol{u}^{\mathrm{w}}(\boldsymbol{x},s)\right]d\boldsymbol{x}_h\right\}ds$$
$$=\sum_{m,n=-N}^{N}\{2\omega_{\mathbf{k}}e^{2kz}$$
$$\times\left[(k_x,k_y,ik)c_{\mathbf{k}}c_{-\mathbf{k}}\left(\frac{\sin(\omega_{\mathbf{k}}T/2)}{\omega_{\mathbf{k}}T/2}+\frac{e^{-i2\omega_{\mathbf{k}}t}\sin(\omega_{\mathbf{k}}T)}{\omega_{\mathbf{k}}T}\right)\right.$$
$$\left.+(k_x,k_y,-ik)c^*_{\mathbf{k}}c_{\mathbf{k}}\left(1-\frac{\sin(\omega_{\mathbf{k}}T/2)}{\omega_{\mathbf{k}}T/2}\right)\right]+c.c.\} \tag{A.40}$$
$$\approx\sum_{m,n=-N}^{N}(k_x,k_y,0)4c_{\mathbf{k}}c^*_{\mathbf{k}}\omega_{\mathbf{k}}e^{2kz}, \tag{A.41}$$

for T sufficiently large ($T\gg\sqrt{2L/\pi g}$). Then the cell-averaged Stokes drift centered at the origin for an arbitrary t yields

$$\boldsymbol{u}^S(0,0,z,t;\boldsymbol{L}_h,T)\approx\sum_{m,n=-N}^{N}4c_{\mathbf{k}}c^*_{\mathbf{k}}\omega_{\mathbf{k}}\mathbf{k}e^{2kz}. \tag{A.42}$$

Now let $\boldsymbol{x}_g$ represent the center of any grid cell (with dimension $\boldsymbol{L}_h$) but with an arbitrary depth z. Then (A.42) can be generalized as

$$\boldsymbol{u}^S(\boldsymbol{x}_g,t;\boldsymbol{L}_h,T)\approx\sum_{m,n=-N}^{N}4c_{\mathbf{k}}c^*_{\mathbf{k}}\sqrt{gk}\mathbf{k}e^{2kz}. \tag{A.43}$$

A.2.4. The Stokes drift spectral density estimate

The spectral density can be reformulated in cylindrical coordinates as

$$\int_{-\infty}^{\infty}\mathcal{S}_{\mathbf{k}}(\mathbf{k})\,d\mathbf{k}=\int_0^\infty\int_{-\pi}^{\pi}\mathcal{S}_{k\theta}(k,\theta)d\theta dk$$
$$=\int_0^\infty\int_{-\pi}^{\pi}\mathcal{S}_{f\theta}(f,\theta)d\theta df. \tag{A.44}$$

These spectral definitions imply relationships according to the Jacobian for a change of independent variables, e.g.,

$$\mathcal{S}_{f\theta}(f,\theta)=\frac{8\pi^2 f}{g}\mathcal{S}_{k\theta}(k=(2\pi f)^2/g,\theta), \tag{A.45}$$
$$\mathcal{S}_{k\theta}(k,\theta)=k\mathcal{S}_{\mathbf{k}}(k_x=k\cos\theta,k_y=k\sin\theta). \tag{A.46}$$

Using (A.23), it follows that the cell-averaged Stokes drift from (A.43) can be rewritten in spectral density form (for $L>1$ km, $T\gg\sqrt{2L/\pi g}$) as

$$\boldsymbol{u}^S(\boldsymbol{x}_g,t;\boldsymbol{L}_h,T)\approx\int_{-\infty}^{\infty}2\sqrt{gk}\mathbf{k}\mathcal{S}_{\mathbf{k}}(\mathbf{k})d\mathbf{k} \tag{A.47}$$
$$=\frac{16\pi^3}{g}\int_0^\infty\int_{-\pi}^{\pi}(\cos\theta,\sin\theta,0)f^3\mathcal{S}_{f\theta}(f,\theta)e^{\frac{8\pi^2f^2}{g}z}d\theta df. \tag{A.48}$$

A.3. Wave spectral separability and simplification

By definition,

$$\int_{-\pi}^{\pi}\mathcal{S}_{f\theta}(f,\theta)d\theta\equiv\mathcal{S}_f(f). \tag{A.49}$$

However, often the wave spectra is split such that

$$\int_0^\infty\int_{-\pi}^{\pi}\mathcal{S}_{f\theta}(f,\theta)d\theta df=\int_0^\infty\int_{-\pi}^{\pi}\phi_f(f,\theta)\mathcal{S}_f(f)\,d\theta df, \tag{A.50}$$
$$=\int_0^\infty\mathcal{S}_f(f)df, \tag{A.51}$$

where the *wave directional distribution*, ϕ_f, satisfies

$$\int_{-\pi}^{\pi}\phi_f(f,\theta)d\theta=1. \tag{A.52}$$

For spectra as in (A.50), it follows that the full Stokes drift from (A.48) becomes

$$\boldsymbol{u}^S(\boldsymbol{x}_g,t;\boldsymbol{L}_h,T)$$
$$\approx\frac{16\pi^3}{g}\int_0^\infty\left[\int_{-\pi}^{\pi}(\cos\theta,\sin\theta,0)\phi_f(f,\theta)d\theta\right]f^3\mathcal{S}_f(f)e^{\frac{8\pi^2f^2}{g}z}df \tag{A.53}$$
$$=\frac{16\pi^3}{g}\int_0^\infty\boldsymbol{H}(f)\,f^3\mathcal{S}_f(f)e^{\frac{8\pi^2f^2}{g}z}df. \tag{A.54}$$

Here, $\boldsymbol{H}$ represents the Stokes drift loss due to wave energy being directed along other directions than the dominant direction, given by

$$\boldsymbol{H}(f)=\int_{-\pi}^{\pi}(\cos\theta,\sin\theta,0)\phi_f(f,\theta)d\theta. \tag{A.55}$$

This will be called the *directional spread loss* here. If in addition, the wave spectrum is separable, then ϕ_f is frequency independent (i.e., $\phi_f=\phi(\theta)$), and (A.54) simplifies to

$$\boldsymbol{u}^S(\boldsymbol{x}_g,t;\boldsymbol{L}_h,T)\approx\frac{16\pi^3}{g}H\hat{\boldsymbol{e}}^{\mathrm{w}}\int_0^\infty f^3\mathcal{S}_f(f)e^{\frac{8\pi^2f^2}{g}z}df, \tag{A.56}$$

with H and $\hat{\boldsymbol{e}}^{\mathrm{w}}$, the magnitude and dominant direction of the directional spread loss. Furthermore, if the wave field in question is unidirectional, i.e., $\phi_f(f,\theta)=\delta(\theta-\theta_f)$ for some wave direction θ_f, then $H=1$ and gives the ($1\mathrm{D}_h$) approximation

$$\boldsymbol{u}^s(\boldsymbol{x}_g,t;\boldsymbol{L}_h,T)\approx\frac{16\pi^3}{g}\hat{\boldsymbol{e}}^{\mathrm{w}}\int_0^\infty f^3\mathcal{S}_f(f)e^{\frac{8\pi^2f^2}{g}z}df. \tag{A.57}$$

It should be pointed out that unidirectionality is a strong assumption and is common in literature (Kenyon, 1969; McWilliams and Restrepo, 1999, etc.). In the third-generation wave model (WW3) used for this study, the weaker assumption of separability provides a reduction by H, or *spread loss* of roughly 75% (global mean). For the Donelan spectrum, $|\boldsymbol{H}(f)|$ is typically larger and ranges from 0.75 to 0.95 (See Appendix A.4).

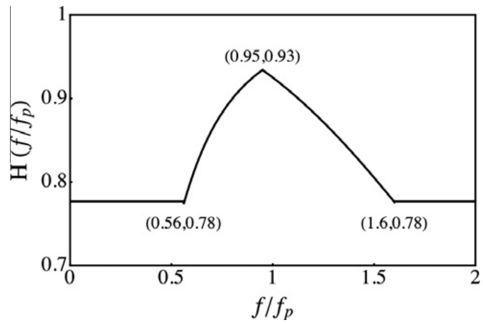

Fig. 5. Directional spread decay H_1 using the Donelan spread function ϕ_f with $\bar{\theta}(f) = 0$.

A.4. Case example: spread loss and Donelan spreading

As stated in Appendix A.3, spreading plays a large role in determining the magnitude of the Stokes drift, even for separable spectra. To illustrate, consider the following hypothetical wave spectra with the same Gaussian distribution across all frequencies,

$$\mathcal{S}_{f\theta}(f,\theta) = \sqrt{\frac{2}{\pi}} e^{-2\theta^2} \mathcal{S}_f(f). \tag{A.58}$$

Then $\hat{e}^w = \hat{e}_1$ and $H = 0.882$.

As another example, consider the normalized, empirically-determined frequency-dependent Donelan spread function (Donelan et al., 1985),

$$\phi_f(f,\theta) = \frac{\beta(f/f_p)}{2\tanh(\beta(f/f_p)\pi)} \operatorname{sech}^2(\beta(f/f_p)(\theta - \bar{\theta}(f))), \tag{A.59}$$

where f_p is the peak frequency and $\bar{\theta}$ is the mean direction for a particular f, and β is given by

$$\beta(f) = \begin{cases} 2.61 f^{1.3} & 0.56 < f \leqslant 0.95, \\ 2.28 f^{-1.3} & 0.95 < f < 1.6, \\ 1.24 & \text{otherwise}. \end{cases} \tag{A.60}$$

Setting $\bar{\theta}(f) = 0$, it follows from (A.55) that $\boldsymbol{H} = (H_1, 0, 0)$ and is bounded by $0.777 \leqslant H_1 \leqslant 0.934$ (see Fig. 5).

A.5. Case example: necessity of spatial averaging

As stated in Appendix A.2.2, there is a direct relationship between the spatial and temporal average of the wave variance and its Fourier transform, magnitude squared, in the frequency and wavevector domain for statistically homogeneous and stationary waves. Thus, spatial averaging is necessary in our derivation of Stokes drift. To illustrate, a simple example is examined. Consider two monochromatic waves traveling in orthogonal directions but with the same wave number magnitude ($|\mathbf{k}_1| = |\mathbf{k}_2| = k$) and initial conditions ($\tau_{\mathbf{k}_1} = \tau_{\mathbf{k}_2} = 0$), given by

$$\eta^w_{\mathbf{k}_1} = a_{\mathbf{k}_1} \cos(kx - \omega_k t) \quad \text{and} \quad \eta^w_{\mathbf{k}_2} = a_{\mathbf{k}_2} \cos(ky - \omega_k t). \tag{A.61}$$

Notice that without spatial averaging, the large T limit of (A.9) yields oscillatory solutions in $\boldsymbol{x}_h$:

$$\lim_{T\to\infty} \left[\frac{1}{T} \int_{t-T/2}^{t+T/2} \left(\int_t^s \boldsymbol{u}^w(\boldsymbol{x}, s') ds' \right) \cdot \nabla \boldsymbol{u}^w(\boldsymbol{x}, s) ds \right] = \left(a_1^2 + \frac{a_1 a_2}{2} \cos k(x-y), a_2^2 + \frac{a_1 a_2}{2} \cos k(x-y), 0 \right) \sqrt{gk^3} e^{2kz}. \tag{A.62}$$

Contrast with (A.43) which has no spatial oscillatory solutions,

$$\boldsymbol{u}^s(\boldsymbol{x}_g, t; \boldsymbol{L}_h, T) = (a_1^2, a_2^2, 0) \sqrt{gk^3} e^{2kz}. \tag{A.63}$$

The required size of spatial averaging may be gauged by wavelength, as is clear from (A.63).

References

Alves, J., Banner, M., Young, I., 2003. Revisiting the Pierson–Moskowitz asymptotic limits for fully developed wind waves. Journal of Physical Oceanography 33, 1301–1323.

Ardhuin, F., Chapron, B., Collard, F., 2009a. Observation of swell dissipation across oceans. Geophysical Research Letters 36. doi:10.1029/2008GL037030.

Ardhuin, F., Marié, L., Rascle, N., Forget, P., Roland, A., 2009b. Observation and estimation of Lagrangian, Stokes, and Eulerian currents induced by wind and waves at the sea surface. Journal of Physical Oceanography 39, 2820–2838.

Banner, M.L., 1990. Equilibrium spectra of wind-waves. Journal of Physical Oceanography 20, 966–984.

Bouws, E. (Ed.), 1998. Guide to Wave Analysis and Forecasting, second ed. Number 702 in WMO, World Meteorological Organization, Geneva, 159 pp.

Caires, S., Sterl, A., Bidlot, J., Graham, N., Swail, V., 2004. Intercomparison of different wind-wave reanalyses. Journal of Climate 17, 1893–1913.

Caires, S., Sterl, A., Gommenginger, C.P., 2005. Global ocean mean wave period data: validation and description. Journal of Geophysical Research-Oceans 110. doi:10.1029/2004JC002631.

Collard, F., Ardhuin, F., Chapron, B., 2009. Monitoring and analysis of ocean swell fields from space: new methods for routine observations. Journal of Geophysical Research-Oceans 114. doi:10.1029/2008GL037030.

Comiso, J., 1999. Bootstrap sea ice concentrations for NIMBUS-7 SMMR and DMSP SSM/I. Technical Report 2, National Snow and Ice Data Center, Boulder, CO (Updated 2008).

Cotton, P.D., Carter, D.J.T., 1994. Cross calibration of TOPEX, ERS-1, and GEOSAT wave heights. Journal of Geophysical Research-Oceans 99, 25025–25033.

Craik, A.D.D., Leibovich, S., 1976. Rational model for Langmuir circulations. Journal of Fluid Mechanics 73, 401–426.

Donelan, M.A., Hamilton, J., Hui, W.H., 1985. Directional spectra of wind-generated waves. Philosophical Transactions of the Royal Society of London Series A – Mathematical Physical and Engineering Sciences 315, 509–562.

Fu, L.L., Christensen, E.J., Yamarone, C.A., Lefebvre, M., Menard, Y., Dorrer, M., Escudier, P., 1994. TOPEX/POSEIDON mission overview. Journal of Geophysical Research-Oceans 99, 24369–24381.

Gommenginger, C.P., Srokosz, M.A., Challenor, P.G., Cotton, P.D., 2003. Measuring ocean wave period with satellite altimeters: a simple empirical model. Geophysical Research Letters 30. doi:10.1029/2003GL017743.

Gourrion, J., Vandemark, D., Bailey, S., Chapron, B., Gommenginger, G., Challenor, P., Srokosz, M., 2002. A two-parameter wind speed algorithm for ku-band altimeters. Journal of Atmospheric and Oceanic Technology 19, 2030–2048.

Gower, J.F.R., 1996. Intercalibration of wave and wind data from TOPEX/POSEIDON and moored buoys off the west coast of Canada. Journal of Geophysical Research-Oceans 101, 3817–3829.

Gulev, S.K., Grigorieva, V., Sterl, A., Woolf, D., 2003. Assessment of the reliability of wave observations from voluntary observing ships: insights from the validation of a global wind wave climatology based on voluntary observing ship data. Journal of Geophysical Research-Oceans 108. doi:10.1029/2002JC001437.

Hanley, K.E., Belcher, S.E., Sullivan, P.P., 2010. A global climatology of wind-wave interaction. Journal of Physical Oceanography 40, 1263–1282.

Hanson, J.L., Tracy, B.A., Tolman, H.L., Scott, R.D., 2009. Pacific hindcast performance of three numerical wave models. Journal of Atmospheric and Oceanic Technology 26, 1614–1633.

Harcourt, R.R., D'Asaro, E.A., 2008. Large-eddy simulation of Langmuir turbulence in pure wind seas. Journal of Physical Oceanography 38, 1542–1562.

Hasselmann, K., Olbers, D., 1973. Measurements of wind-wave growth and swell decay during the Joint North Sea Wave Project (JONSWAP). Erg "anzung zur Deut. Hydrogr. Z., Reihe A (8) 12, 1–95.

Hasselmann, K., Ross, D.B., Muller, P., Sell, W., 1976. Parametric wave prediction model. Journal of Physical Oceanography 6, 200–228.

Hemer, M.A., Church, J.A., Hunter, J.R., 2010. Variability and trends in the directional wave climate of the Southern Hemisphere. International Journal of Climatology 30, 475–491.

Janssen, P.A.E.M., Doyle, J.D., Bidlot, J., Hansen, B., Isaksen, L., Viterbo, P., 2002. Impact and feedback of ocean waves on the atmosphere. In: Perrie, W. (Ed.), Adv. Fluid. Mech, Atmosphere–Ocean Interactions, vol. I. Elsevier, pp. 155–195.

Kantha, L., Clayson, C., 2004. On the effect of surface gravity waves on mixing in the oceanic mixed layer. Ocean Modelling 6, 101–124.

Kenyon, K.E., 1969. Stokes drift for random gravity waves. Journal of Geophysical Research 74, 6991–6994.

Kitaigorodskii, S.A., 1983. On the theory of the equilibrium range in the spectrum of wind-generated gravity-waves. Journal of Physical Oceanography 13, 816–827.

Komen, G., 1987. Energy and momentum fluxes through the sea surface. In: Proceedings of the Fourth 'Aha Huliko'a Winter Workshop on Dynamics of the Ocean Surface Mixed Layer, University of Hawaii at Manoa, Honolulu, HI, pp. 207–217.

Kundu, P.K., 1990. Fluid Mechanics. Academic, San Diego, Calif., 638 pp.

Large, W.G., Yeager, S.G., 2008. The global climatology of an interannually varying air–sea flux data set. Climate Dynamics 33, 341–364.

McWilliams, J., Restrepo, J., 1999. The wave-driven ocean circulation. Journal of Physical Oceanography 29, 2523–2540.
McWilliams, J.C., Sullivan, P.P., Moeng, C.H., 1997. Langmuir turbulence in the ocean. Journal of Fluid Mechanics 334, 1–30.
Ochi, M.K., 1998. Ocean Waves: The Stochastic Approach, vol. 6. Cambridge University Press, Cambridge, UK, 319 pp.
Phillips, O.M., 1958. The equilibrium range in the spectrum of wind-generated waves. Journal of Fluid Mechanics 4, 426–433.
Phillips, O.M., 1966. The Dynamics of the Upper Ocean. Cambridge University Press, Cambridge, 344 pp.
Pierson Jr., W.J., Moskowitz, L., 1964. A proposed spectral form for fully developed wind seas based on the similarity theory of S.A. Kitaigorodskii. Journal of Geophysical Research 69, 5181–5190.
Rayner, N., Brohan, P., Parker, D., Folland, C., Kennedy, J., Vanicek, M., Ansell, T., Tett, S., 2006. Improved analyses of changes and uncertainties in sea surface temperature measured in situ sice the mid-nineteenth century: the HadSST2 dataset. Journal of Climate 19, 446–469.
Stewart, R.H., 2008. Introduction to Physical Oceanography. Printed by author, Texas A & M University, 345 pp.
Tolman, H.L., 2009. User manual and system documentation of WAVEWATCH-III version 3.14. Technical Report 286, NOAA/NWS/NCEP/MMAB, 220 pp.
Townsend, T., Hurlburt, H., Hogan, P., 2000. Modeled sverdrup flow in the north atlantic from 11 different wind stress climatologies. Dynamics of Atmospheres and Oceans 32, 373–417.
Uppala, S., Kallberg, P., Simmons, A., Andrae, U., Bechtold, V., Fiorino, M., Gibson, J., Haseler, J., Hernandez, A., Kelly, G., Li, X., Onogi, K., Saarinen, S., Sokka, N., Allan, R., Andersson, E., Arpe, K., Balmaseda, M., Beljaars, A., Van De Berg, L., Bidlot, J., Bormann, N., Caires, S., Chevallier, F., Dethof, A., Dragosavac, M., Fisher, M., Fuentes, M., Hagemann, S., Holm, E., Hoskins, B., Isaksen, L., Janssen, P., Jenne, R., McNally, A., Mahfouf, J., Morcrette, J., Rayner, N., Saunders, R., Simon, P., Sterl, A., Trenberth, K., Untch, A., Vasiljevic, D., Viterbo, P., Woollen, J., 2005. The era-40 re-analysis. Quarterly Journal of the Royal Meteorological Society 131, 2961–3012.
Webb, A., Fox-Kemper, B., Baldwin-Stevens, E., Danabasoglu, G., Hamlington, B., Large, W.G., Peacock, S., in preparation. Global climate model sensitivity to estimated Langmuir mixing. Ocean Modelling.